Review of Atmos. Meas. Tech. Manuscript (#amt-2019-439) "Calibration of an airborne HOx instrument using the All Pressure Altitude based Calibrator for $HO_X$ Experimentation (APACHE)" by D. Marno et al.

We are thankful to the reviewer for the helpful and constructive comments.

**General Comments**

In this work, a new airborne HOx calibration system was developed and evaluated to mimic the conditions (e.g., varying pressure, temperature, and humidity) during a typical flight. This kind of work is important to determine the response of HOx instruments for the accurate airborne measurements of OH and $HO_2$, which is the key to understand the atmospheric photochemistry. A computational fluid dynamics model (COMSOL) was used to simulate the fluid dynamics in the calibrator. Two actinometric methods based on the photolysis of ozone and N2O (used in ground-based calibrator) were used to determine the actinic flux of the mercury lamp that is used to generate OH and HO2. Overall I found this manuscript needs major revisions. The difference in actinic flux measurement using the two methods is quite large. I would suggest conducting the actinic flux measurement in APACHE using the photolysis of N2O to rule out any uncertainties in transferring the ground calibration to airborne calibration. Section 5 is particularly lean and not well organized. More details and discussion should be included in this section (see details below). I also found many errors in equations and units and tried to point most of them out. Please check out the entire manuscript. I would ask the authors to consider the following special comments in their revision.

In light of the comments provided, we have made changes and provided clarification to the paper. Regarding the actinic flux measurements, we originally considered the lamp being a point source, which is wrong as the diameter of the lamp tube is 19mm. When considering the lamp as an respectively extended source of light with the corresponding beam profile we achieve a convergence between the two flux measurements with the HORUS transfer standard flux of 6.9 (± 1.1) $x10^{14}$ photons $cm^{-2}$ $s^{-1}$, and the Ozone experiment yielding 6.11 (± 0.8) $x10^{14}$ photons $cm^{-2}$ $s^{-1}$. The agreement between the two experiments have improved from a zeta score of 0.88 to 0.59, with the overall flux value being 6.37 (± 1.3) $x10^{14}$ photons $cm^{-2}$ $s^{-1}$. This value is calculated by taking the average of the two methods weighted by their uncertainties. Section 5 has been merged with section 4, as we feel that the whole of section 4 entails results and discussion. Discussed elements that were in section 5 have been organized and expanded upon, please see comments and revised document.

**Special Comments**

1. L.18: For ground-based HOx instruments … (remove systems)

   Deleted "Systems"

2. L.26: Define COMSOL at its first appearance.

3. We have described COMSOL as a computational fluid dynamics model. Its origin is FEMLAB, a former toolbox of Matlab, which name is derived from 'Finite-Element-Method-Laboratory'.
4. L.47: "Other methods have also been … (Remove "However")

   Removed "However"
5. L.48: the CIMS work by C. Cantrell and L. Mauldin should also be cited here.

   "Cited C. Cantrell and L. Mauldin" .
6. L.61-69: Start this with a new paragraph. At the end of this paragraph (or maybe start a third paragraph), you might want to mention what was done in this work (e.g. establishment and evaluation of the APACHE, etc.)

   Now is a separate paragraph. Containing what was done in this work.
7. L.75: Define APACHE at its first appearance in the main text even though you have defined it in the abstract.

   Defined APACHE in its first appearance in the main text.
8. L.92: Figure 2 (capital F). Please check this throughout the manuscript.

   All references to a figure or table in text or otherwise have been capitalized as Figure or Table.
9. Fig. 1: "Controlled humidity airflow of 300 sccm": is the 300 sccm of humidified air is enough to vary the humidity in the total flow of 200-900 sL/min mentioned in L.105?

   Typo. It was 300 sL $min^{-1}$. Figure corrected.
10. Caption of Figure 1: Maybe change it to "Overview of the APACHE system and the premixing setup. A picture at the bottom shows the perforated stainless steel plates with wool mesh."

    Changed caption for Figure 1.
11. L.107: The word "respectively" is used but the air speed changes by a factor of less than 2 (0.9 to 1.5 m/s) while the pressure changes by a factor of 4 (from 250 to 1000 mbar). I understand the total mass flow rate was adjusted accordingly. Please clarify this and

    maybe remove respectively and say the pressure **from** 250 **to** 1000 mbar. Also because of ram effect during flight due to the installation of a choke point in the shroud (L.131) , the ambient air pressure can potentially more than 1000 mbar. Have the calibration system tested a little over 1000 mbar?

    During testing it was found that APACHE is capable of operating at pressures exceeding 1000 mbar. However, the main focus of this study was to investigate APACHE operation to calibrate the HORUS instrument for the HALO (High Altitude Long Range) aircraft at altitudes above the boundary layer. Only below 1.5km the pressure is due to the ram pressure larger than 1000 mbar
12. L.168, **where,** $W_{z1\ pwr}$ is …

Added "Where,"

13. Eq. (1) and (2): I would suggest using [OH] and [$HO_2$] for OH and $HO_2$ mixing ratios or concentrations. Please check this out for the entire manuscript. Also it seems to me that the last term ($C_{OH(2)}/C_{OH}*S_{OH}$) needs to take the laser power in the first and second axes into account (unless $Wz1_{power}$ and $Wz_{2\ power}$ are the same, which is unlikely) and assume there is little OH loss between the 2 axes. The OH signal in the second axis ($S_{OH(2)}$) should be:

    $S_{OH(2)} = [OH]*C_{OH(2)}*Wz_{2\ power} = S_{OH}/(C_{OH}*Wz_{1\ pwr})*C_{OH(2)}*Wz_{2\ power}$

    Please check and correct this.

    Checked and agree with the proposed changes.

14. L.179: I believe the term $Wz_{pwr}$ the should be a denominator in Eq.(4) as the units for $C_{OH}$ should be cts $cm^3$ $molecule^{-1}$ $s^{-1}$ $mW^{-1}$. Also here $cm^3$ $molecule^{-1}$ is used, while in L.170 $pptv^{-1}$ is used. Please be consistent and check this out for the entire manuscript.

    Eq. (4) has been adapted with the consideration of the following:

    The c0 coefficient actually has the units (cts $pptv^{-1}$ $s^{-2}$ $cm^3$ $molecule^{-1}$ $mW^{-1}$) i.e in calibrations it is normalized by laser power, Boltzmann correction, quenching (s), internal density (molecules $cm^{-3}$). During flight and c0 is multiplied by Boltzmann correction, quenching (s), internal density (molecules $cm^{-3}$) resulting in the sensitivity $C_{OH}$ having the units cts $s^{-1}$ $pptv^{-1}$ $mW^{-1}$. $C_{OH}$ is then scaled by the actual power measured in flight resulting in the units, cts $s^{-1}$ $pptv^{-1}$. Then the averaged 5 Hz measured signal (averaged to cts in a second) during flight (see Eq. 1) is subsequently divided by the laser power scaled $C_{OH}$, resulting in the units pptv for OH.

15. L.189: White cell (capital W)

    Capitalized W.

16. L.199: again the units in the denominator are not correct because C0 has units of cts $cm^3$ $molecule^{-1}$ $s^{-1}$ as mentioned in L.183, assuming $S_{OH}$ has units of cts $s^{-1}$.

    See comment 13. Units for c0 was not correctly described.

17. L.206: see the above comment for the issue of units.

    See comment 13.

18. Caption of Figure 3: **dash-dotted** blue line and **dashed** red line.

    Corrected.

19. L.211: Table 1 (capital T)

    Capitalized the T.

20. L.213: change pure to purified.

    Pure in this statement means that only synthetic air is used to calibrate with. I.e. no other type of gas is used as a medium. We have changed "pure" to "only" to emphasize that only syn air is used as the medium for calibration.

21. L.241: the units for $F_{184.9\,nm}$ should be photons **cm$^{-2}$** s$^{-1}$.

    Units corrected to photons cm$^{-2}$ s$^{-1}$.

22. L.288-289: were the air flow speed profiles measured at different pressures, e.g., such as pressures lower than 920 mb to simulate conditions at high altitudes during flight?

    With pressures below 920 mbar, the reading from the differential pressure sensor was close to or below its resolution. Hence the need to utilize other methods to parameterize the flow conditions within APACHE.

23. L.297: Spell out COMSOL.

    Defined COMSOL again as a computational fluid dynamics model (CFD).

24. L.309-315: the disagreement could also be due to the uncertainty in the COMSOL model simulation.

    Added a comment stating this.

25. Figure 6: the air flow speed within APACHE is really unified, even close to the wall. This is good.

26. L.316: do you mean discrete instead of discreet?

    Yes, this is a misspelling.

27. Caption of Figure 7: "The black arrows depict the flow direction." It is hard for me to see those arrows. Maybe include a big arrow on each plot to show the flow direction instead?

    We have increased the arrow size to make them clearer.

28. L.361: Please add "In Table 2" at the beginning of this sentence.

    Added Table 2

29. L.362: streamline (remove s or use streamlines in other places)

    By this, we mean literally on the leftmost streamline for L or rightmost streamline for R, C is in the middle of the streamlines. We have checked that such plural or singular usage is consistent.

30. L.366: **F**igure 8 and **T**able 2

    Capitalized

31. L.368: **On** the APACHE walls.

    Changed "at" to "on".

32. L.377: "between **the lamp** and a quartz wall" to be clear.

    Agreed and applied the change.

33. L.392-392: Martinez et al., 2010 is referred here, but I think at least a brief description of the ground-based calibration system should be given, especially the method to determine the actinic flux of the Hg lamp using the photolysis of N2O to provide the context for Table 3. Otherwise readers may have no idea why NO monitor/N2O cross section are suddenly mentioned in Table 3.

We have included a short description and equation with reference to Martinez et al., 2010, showing where the NO monitor and NO standard terms in table 3 are coming from.

34. Later I found the difference of the two methods is quite large (~20%). I wonder if it is possible to conduct the actinic flux measurement in APACHE using the photolysis of N2O directly so that any uncertainties in transferring the ground calibration to airborne calibration will not affect this difference.

    The difference in the original flux values may appear large however, given their uncertainties the zeta score was 0.88, suggesting agreement within the combined uncertainty of both measurements. However, in light of the comments and suggestions, the calibrations and terms therein have be checked, reevaluated and adjusted when considering the lamp as an extended source of light with a corresponding beam profile. By doing this, the two methods converge, 6.9 (± 1.1) $x10^{14}$ photons $cm^{-2}$ $s^{-1}$ for method A, and 6.11 (± 0.8) $x10^{14}$ photons $cm^{-2}$ $s^{-1}$ for method B. The agreement between the two experiments has a zeta score of 0.59, meaning they agree to within 59 % of one sigma of their combined uncertainties, suggesting agreement.

35. L.397: "…when the smaller 0.8 mm critical **orifice** was used."

    Added "orifice".

36. L.418: Do these OH and $HO_2$ occur inside APACHE during the transport of air flow from the UV radiation zone and HORUS inlet? Please specify.

    Yes, we calculate this based on the recommended reaction rates, number densities occurring in APACHE, and the calculated transit times that occur in APACHE between the lamp and the HORUS inlet.

37. L.426: Duplicate definition as this has been defined in L.235.

    The equation is used again here as the discussion is building up from it. We believe it is easier for the reader to follow the discussion if they do not have to flip back several pages to check what is being referred to in this section of the discussion.

38. L.457: units for $F_\beta$ should be photons $cm^{-2}$ $s^{-1}$.

    Corrected the units

39. L.458: Table 3 should be referred here.

    Table 3 in now referred here.

40. L.459-460: Martinez et al., 2010 should be referred here.

    Martinez et al., 2010 in now referred here.

41. Section 5: Results and Discussion: this section is very lean. Some results in Section 4 could go into this section (e.g., the results for the two methods to determine the Hg lamp actinic flux). There is also no mention how the individual measurements of overall sensitivity ($1^{st}$ row of Figure 10) are used to calculate OH and HO2 mixing ratios in the real airborne measurements. For example, the $HO_2$ sensitivity in the $2^{nd}$ axis varied by a factor of 2 (20 vs. 10 cts/s/pptv/mW) at the internal density of 1.5E17 $cm^{-3}$. What sensitivity to use for the real measurements with internal densities between these two

calibration points? Also any plan/future work to conduct more calibrations to get a better statistics and possibly to draw a smooth calibration fitted line as a function of internal pressure as shown in Figure 3?

Section 5 is now merged with section 4, with some aspects expanded upon. We have included a description and equation showing how the c0, c1,c2 (otherwise labelled as a grouped term cN in the figure) are calculated.

In row A Figure 10 we have decided to provide a smoothed calibration curve much like the one shown in figure 3. Once c0, c1,c2 are known, and quenching, internal density and transmission efficiency are quantified with consideration of the measured internal temperatures and pressures, one can use equation 4, to adequately resolve the sensitivity within 2 sigma of the uncertainties. These points have been added into section 4.3.1. Additionally we have included a paragraph clarifying how these terms are then used to quantify the sensitivity for airborne measurements. Figure 11 has been included to show how sensitivity, $HO_X$ transmission and detection limits look like when quantified using measured temperatures and pressures values in HORUS under flight conditions .

42. L.489: Table 6 is mentioned before the appearance of Table 5.

    Table 5 is now mentioned before mentioning Table 6.

43. L.495: "…resulting in **the transmission** for both OH and $HO_2$ to be…"

    Added "the transmission".

44. L.498: ".. the time it takes **for** air to flow…"

    Added "for".

45. L.522-526: this paragraph is out of the context of this section. I would suggest moving this paragraph and some actinometric results in Section 4 to a new subsection of 5.2.

    Paragraph moved to calibration uncertainty section, 4.3.2. Where a fuller discussion regarding uncertainty is present.

46. L.524-526: Again units for $F_\beta$ should be photons $cm^{-2}$ $s^{-1}$ or $cm^{-2}$ $s^{-1}$.

    Changed to units for $F_\beta$ to photons $cm^{-2}$ $s^{-1}$ or $cm^{-2}$ $s^{-1}$.

47. Again I would suggest conducting the actinic flux measurement in APACHE using the photolysis of $N_2O$ directly.

    Addressed in previous sections, and opening statement

48. Section 5.2. Absolute Calibration Uncertainty: this section is very lean and more discussion can be included

    This section has been incorporated into the Evaluation of instrumental sensitivity section. In hindsight, we believe that it is clearer for the reader to follow the discussion and to realize where the uncertainties are sourced from and to what scale they impact the final sensitivity values.

49. L.531: **T**ables 5 to 8.

    Capitalized T

50. Table 5: units for $F_\beta$ should be photons $cm^{-2}$ $s^{-1}$ or $cm^{-2}$ $s^{-1}$. Also a temperature range of 282-302 K is given but no mention in the text how it was varied within APACHE.

    Temperature ranges now discussed in section 2.2

51. Table 7: this should go Section 5.1 where transmissions are discussed.

    See comment 47.

52. Table 6 and the 3rd row in Figure 10: details about how the term cN* internal density is calculated/measured should be given.

    Included equation and discussion regarding how cN is calculated se Eq 14.

53. L.559, and 562: the actinic flux of the mercury lamp should be photons $cm^{-2}$ $s^{-1}$.

    Corrected the units

54. Figure 10: the 1st row: the units should be cts $\mathbf{s^{-1}}$ $pptv^{-1}$ $mW^{-1}$.

    Corrected the units

55. Figure 10: "Row C is (C) is internal density and cN". Do you mean "Row C is the product of internal density and cN"? I don't understand how cN is calculated.

    Included equation and discussion regarding how cN is calculated see Eq. 15,16 and 17.

Atmos. Meas. Tech. Discuss., doi:10.5194/amt-2019-439-RC2, 2020 

Atmospheric Measurement Techniques Discussions

# *Interactive comment on* "Calibration of an airborne $HO_X$ instrument using the All Pressure Altitude based Calibrator for $HO_X$ Experimentation (APACHE)" *by* Daniel Marno et al.

**Anonymous Referee #2**

Received and published: 18 January 2020

In this paper Marno et al. demonstrate the first results from the "APACHE" chamber designed to calibrate and characterise the Mainz airborne "HORUS" OH and HO2 instrument. The results show the APACHE chamber operating on the ground under controlled conditions to calibrate HORUS, but it is designed also to be operated on the HALO aircraft when OH and HO2 measurements will be made, in order to calibrate in flight.



The development of a device to calibrate for OH and HO2 measurements in flight is a very difficult challenge, not only does the sensitivity of the instrument vary with a change in the pressure and temperature sampled (which changes with altitude),and also the level of water vapour, but also the losses between the point of OH and HO2 generation in the calibrator and sampling by HORUS change also (there would be losses also for ambient OH and HO2 which are to be measured). For the former, the change in sensitivity owing to changes in parameters with altitude after the HORUS inlet can be experimentally determined via the calibration – but in this paper these are investigated through calculations also. For the latter, i.e. losses in OH from the point of generation (lamp) and the HORUS inlet need to be characterised experimentally – and understood. CFD calculations are used to simulate the flowfield within APACHE for comparison with experiment.

The description of a device to generate known concentrations of OH and HO2, and its characterisation and comparison with simulations, given the range of parameters, is complex. Likewise the sensitivity of the instrument measuring OH and HO2 and how this varies with sampling pressure is also complex – and so naturally this paper is complex and many parameters have to be explained and how they change with pressure explained. However, this is critical, as OH and HO2 are highly reactive and can be lost both in the gas-phase and at surface. The authors have made the paper fairly clear – as the characterisation is quite complex – but some further clarity is needed. The experiments appear to have been carefully performed, and many of my comments are aimed to help improving clarity for the reader.

It is not clear from the paper whether the APACHE/HORUS device has been used in flight already, as this reports experiments done in a controlled environment on the ground – and perhaps something about how it performs in flight would be useful to include, and comparison with the ground performance. The paper is an impressive piece of work – and the APACHE/HORUS is quite a feat of engineering and the thorough characterisation of APACHE and HORUS is critical to give confidence in the OH and HO2 measurements from HORUS on HALO. The paper is suitable for AMT, and the development of a calibration source for use inflight for OH measurements is very important, and a considerable achievement. There is a lot covered in this paper, but

some further details/clarifications are needed in some places. See comments below.

More specific comments.

Abstract.

A key result is that the two actinometric approaches agree fairly well, and as well as the average it would be good also to give the level of agreement also. Say what the two approaches are. What pressure is relevant for the value stated, as you say "depending on pressure", which is not clear?

Stated what the two approaches are, their values, and agreement in the form of zeta score. We have removed the mention of pressure as the actinic flux of the lamp is not pressure dependent, this information is discussed at greater length in the text. Not relevant here in the abstract.

Although the paper is about APACHE and its characterisation, I think readers will want to know what the sensitivity is of HORUS determined with APACHE. Could the expected C factors be stated for OH and HO2, and the derived limits of detection, and how these are predicted to vary with altitude, also be given in the abstract.

The overall accuracy of the calibration ought to be stated also in the abstract from the use of APACHE. This is given in some detail in the paper but there is nothing here. A few more numbers summarising actual performance needed in the abstract.

We have included sensitivity values and the calibration accuracy. Regarding the limits of detection we have included a figure and discussion at the end of the paper, describing how they changing during flight.

Also, "controlled environment" is a bit unclear, please make clear that this is on the ground, rather than results being presented of APACHE used under "a controlled environment" on the aircraft in flight.

We have stated here that calibrations with APACHE were performed in the lab.

Introduction.

46. The referencing is rather selective, please also include Juelich and Leeds LIF references (zeppelin and aircraft measurements also). For CIMS include some Eisele group references also (and subsequent including Mauldin/Cantrell which have also flown).

Included these references

Figure 1. The APACHE shown here is for the controlled environment on the ground – make clear in the figure caption. Looking at Figure 2, the left hand side of APACHE would be a bit different when on the aircraft? (no inflow from mixing blocks?)

We do not characterize the inlet shroud, but the HORUS instrument starting at the inlet(IPI Nozzle). In APACHE we provide a homogenous flow profile with a characterized OH profile to HORUS.

96, replace "being" with "is"

Replaced "being" with "is".



107. Is the 0.9 to 1.5 ms-1 in APACHE over the pressure range the same as the flow velocity at the same pressure when sampling on the aircraft. In line 132 the "choke" on the aircraft nacelle is used to lower the flow velocity to < 21 ms-1, but not clear if < 21 ms-1 means it will be similar to the 0.9-1.5 ms-1 as in the controlled experiments on the ground? < 21 ms-1 could cover a wide range.

We have looked into periods during take-off and landing where there are large changes in flow speed (1 to 12 m $s^{-1}$) within the shroud and we find no change in our signal that is attributable to flow speed changes across the IPI nozzle. Therefore, there is no uncharacterized loss, at a detectable level, occurring at the IPI Nozzle when flow speeds are 0.9-1.5 m $s^{-1}$ in APACHE when compared to 21 m $s^{-1}$ during flight.

124 – say also there is a critical orifice at the end of the IPI, this was not clear (and not labelled in Figure 2).

Improved the labelling in figure 2.

There is both a HORUS inlet, and a IPI critical orifice, and I think the presence of these two needs to be clearer. In figure 2 I suggest, that both the HORUS inlet and also the IPI critical orifice have a label. Also both "IPI orifice", "HORUS inlet" and "IPI critical orifice" are used. In line 128, is "IPI orifice" the "HORUS inlet" which samples from APACHE, or the "IPI crictical orifice" which is between the IPI and the 2 fluorescence cells? I think the former as the choke point is then mentioned which slows the flow from the aircraft speed to a slower flow in APACHE?

The IPI nozzle/ inlet is not a critical orifice. The critical orifice sits between IPI itself and the first detection cell. The choke point is at the end of the inner inlet shroud. We have changed the labelling throughout the paper to ensure consistency.

132. "sample velocity of HORUS", this means the flow within APACHE at which HORUS sampled perpendicularly? Is 44-53 ms-1 what is expected on the aircraft? Figure 2. label the critical orifice in the IPI and also HORUS inlet for clarity (as discussed above).

This means the sample flow speed within IPI ranged between 44-53 ms-1 during flight. We have also include at the end of this paragraph a statement explaining that the location of the critical orifice allows HORUS to sample (~ 3 - 17 sL $min^{-1}$) from the central flow that is moving through IPI (~ 51 - 230 sL $min^{-1}$) . The excess flow is removed via a perforated ring that surrounds the base of the critical orifice cone evacuated by a blower. All discussion in section 2.3 is regarding parameters and occurrences during flight. We have also included "during flight" statements here to emphasize we are talking about processes happening in and around HORUS when airborne. We have also adjusted the labelling in Figure 2 (see above).

144. As an IPI is used, it would be worth mentioning OH-WAVE (on to off resonance) and OH-CHEM, otherwise not clear of the purpose of the IPI. All the experiments performed here are OH-WAVE – presumably results of OH-CHEM in a controlled environment (to show all OH removed etc.) will be discussed in another paper. The IPI is present here but not used.

We have included the OH-WAVE and OH-CHEM discussion here. IPI was operated during calibrations as it would have been during flight as it does impact the overall sensitivity. But, as you have indicated, the inflight performance of IPI with regards to scavenging efficiency and OH-CHEM in flight will be discussed in a different publication. For this paper OH-CHEM is not the focus.

149. Again the referencing of papers is selective to a couple of groups only who use LIF.

We have included primary references that discuss directly the OH absorption spectrum. We have left the LIF references because at this point we are only discussing HORUS as a LIF instrument.

C4

153. Quantitative conversion is mentioned here. can a % be given, as it is not possible

to achieve 100% owing to OH+NO + M = HONO + M meaning that not all of the HO2 conversion to OH remains as OH. What is the % that is achieved here? What flow of NO is added?

We have calculated the internal HONO formation in our instrument using the caaba/mecca box model initializing with HO2 and NO at the corresponding low pressure conditions experienced in flight. Note that here any reference to [OH] is in regards to OH formed from the reaction of HO2 with NO. The following figure shows the fractional HONO concentrations formed compared to the formed OH concentrations at different flight altitudes i.e. [HONO] from the reaction $k_{OH+NO+M}$[NO][OH][M] divided by [OH] from $k_{HO2+NO}$[$HO_2$][NO]. This is to show at flight altitudes of 14 km, 9 km, 8 km and 3.5 km what percentage of OH formed from $HO_2$ + NO undergoes further reaction forming HONO internally within HORUS. The black dotted-dashed line is the maximum NO concentration (1.04 x$10^{14}$ molecules $cm^{-3}$) injected into HORUS when we are performing in-flight NO titrations. The blue dotted-dashed line shows the maximum NO concentration (0.79 x$10^{14}$ molecules $cm^{-3}$) injected into HORUS when performing normal measurements, the red dotted-dashed line shows the minimum NO concentration (6.61 x$10^{12}$ molecules $cm^{-3}$) injected into HORUS. When measuring we toggle our NO injection between these two

concentrations to resolve for $RO_2$ interference. At the low NO mode any RO2 interference in the signal is heavily suppressed as there is not sufficient NO present in HORUS to promote production of OH via RO2+NO. The higher NO addition has a better signal to noise ratio, however contains a more significant RO2 contribution. To resolve for this we perform NO titrations to resolve our HO2 conversion efficiency at every pressure level and NO concentrations being injected into HORUS. If the high NO injection signal (once corrected for conversion efficiency) is significantly higher (i.e. consistently above by more than the detection limit) than the low NO concentration signal (once corrected for conversion efficiency) we use the signal from the low NO injection mode for atmospheric HO2 measurements. If the high NO injection is not greater than the low NO injection mode ( i.e. higher by more than the detection limit of HORUS) we use the high NO injection mode as the signal to noise ratio is better.

When titrating to maximum NO concentrations, 3.3 % of formed OH is converted into HONO at 14 km, 5.4 % of formed OH is converted into HONO at 9 km, 7.8 % of formed OH is converted into HONO at 8 km, and 13.8 % of formed OH is converted into HONO at 3.5 km. These values are the upper limit of HONO formation, as the calculations assume perfect mixing of NO. Additionally in this figure for all altitudes, the low NO injection measurement mode results in less than 0.5 % of the formed OH being lost via HONO formation, which further limits the influence of HONO formation on the HO2 signal.

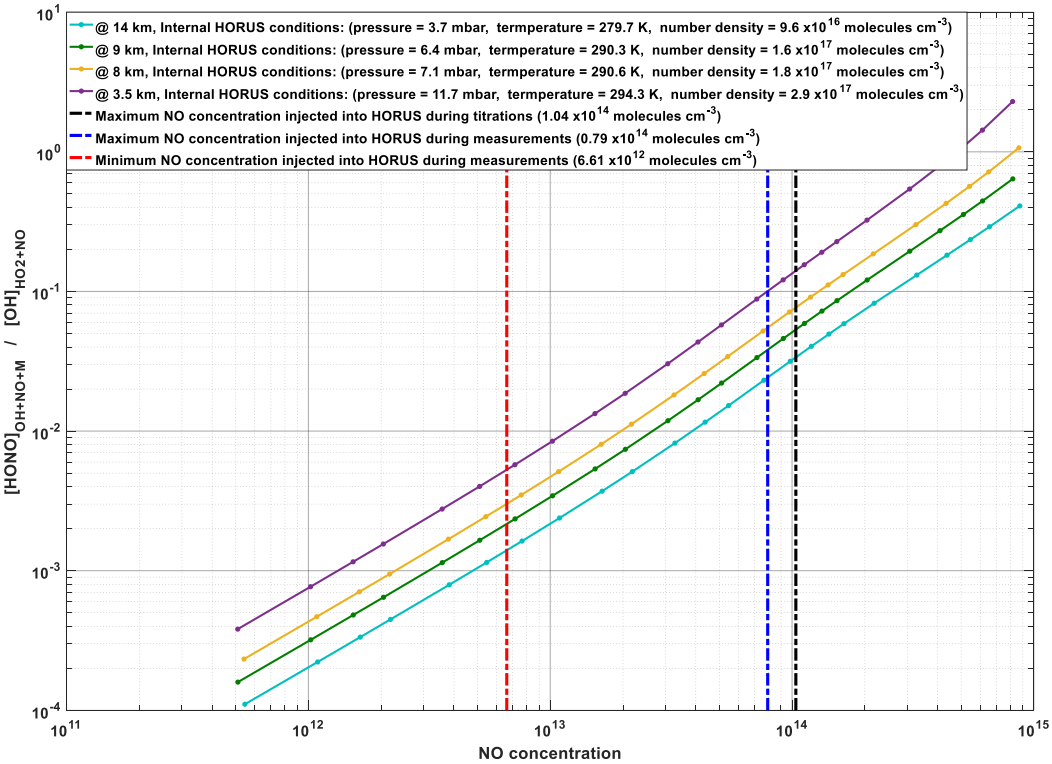


We have also determined what NO concentrations are required to cause HONO formation to have a detectable influence on the HO2 signal in HORUS, i.e. at what NO concentration does the drop in [OH] (caused by HONO formation) from the maximum titrated OH concentration value exceed the detection limit of the instrument. The table below shows these values:

| Altitude (km) | Required NO concentration in HORUS ($x10^{14}$ molecules $cm^{-3}$), to cause HONO formation to have a detectable influence |
|---|---|
| 14 | 2.36 |
| 9 | 1.52 |
| 8 | 1.14 |
| 3.5 | 0.82 |

Note: The NO concentration values quoted here are the lower limit, as these are calculated under the assumption of perfect NO mixing, and taking the minimum characterized detection limit at each altitude level.

This table shows that given the strong pressure dependence of the termolecular reaction that forms HONO, significantly higher NO concentrations (>14% than the maximum titrated concentration) are required to result in a detectable influence on the $HO_2$ signal via HONO formation. Only at flight altitudes 3.5 km and below can HONO formation have a detectable influence. However, this is only in the cases when we are titrating at these low altitudes which is not the main focus of the OMO-ASIA 2015 campaign in which HORUS took part and this study, where the main focus was and is on altitudes exceeding 8 k km. Even in the high HO2 conversion mode, applying NO in the order of 0.79 $x10^{14}$ molecules $cm^{-3}$, the HONO formation still falls below this lower limit.

This discussion regarding HONO forms part of a later publication where instrument performance (e.g. OH-CHEM and $RO_2$ interferences etc) is the focus. Alongside intercomparison with the LIF instrument from Jülich. As the too flew on HALO during the same OMO-ASIA 2015 campaign.

180 “where” small w

Changed to lower case w.

202 – state the size of the critical orifice here. (diameter)

Stated the diameter. 1.4 mm.

Fig 3 – make clear this is a schematic only – rather than any actual performance of the HORUS. Could point to fig 10 where this is shown. Also in the caption, the dotted blue line is for “OH transmission”, whereas in the figure it is “wall loss”.

Corrected the labelling in the figure. Explicitly describe it as a schematic.

219 – split – and 1 in the units

Corrected.

230. Juelich showed that the reaction of H* with O2 did not lead to OH, rather that 100% of H went to HO2, so worth referencing that.

Added Jülich reference.

Table 1. For (IV) CSTR, was the OH generated through UV irradiation of the VOC, or of another precursor? Certainly the decay rate of the VOC is used to determine the OH. Also reference Winiberg et al. 2015 (in the reference list) who used the decay of a hydrocarbon to calibrate for OH in a chamber with a LIF instrument (agreeing well with method I, water paper photolysis).

We have altered the description to match how they are described in the referenced publications. Added Winiberg et al., 2015 to the reference list, including what hydrocarbons were used in that study.

238, “where”, small w

Changed to lower case w.

268. The exhaust from the pumps are at a different pressure when in flight compared to when the exhausts are exposed 1 atm, and this is taken account of by matching to ambient pressures in flight – that is good. Was the same pumping system used for the APACHE testing on the ground as the pumps that will be used (or are used) in flight (which might be 400 Hz pumps from the aircraft power)? (different pumps or pumps used with different motors may have different capacities).

Clarified here that the pumps used during calibrations with APACHE are the same ones that were installed on the aircraft. Also that we used a 3 phase mission power supply unit that provides the same power as on the aircraft.



305 “from the measured...”

Corrected

Figure 6. Can it made clear what is meant by “internal wall of APACHE”, perhaps by cross-referencing to figure 1?

We added a small caption in figure 6 showing what we mean by Internal wall of APACHE

240. The number of sig figs in the error 179 +/-20 does not seem consistent with the sig figs quoted in the errors in brackets for the other units.

Changed the sig figs, so that they match.

361. L, C, and R term are introduced, to make clearer, say which figure they are in – otherwise not clear what referring to.

Clarified in what sense to the L, C and R terms relate to, i.e the streamlines created by the HORUS sample flow in figure 7 and 8.

371. How is 22.2 % loss known for OH and HO2 the inlet? (HORUS inlet). Also, one might expect the loss to be higher for the more reactive OH? Please expand a little.

We have adapted our discussion regarding this variable. According to the model irrespective of pressure the IPI nozzle is 22 %, suggesting that this loss is pressure independent. This value is not utilized any further. The true/characterized/measurable pressure independent loss is now characterized within the pressure independent sensitivity coefficients, which do differ between OH and HO2 at the second axis.

Figure 8. What [H2O] the same for all the pressures? Perhaps add this value.

We have included the water mixing ratio. It was kept constant at 3.2 mmol/mol.

Tabel 2. Right hand column – OH (ppt) also?

Yes pptv. Units added to this column.

395. The IPI critical orifice diameter is given here – but needs to be given earlier as well when this orifice is first introduced. What is the reason that the diameter of this orifice is changed from 1.4 mm to 0.8 mm for the controlled experiments on the ground?

This adaptation was done to enable use to relate the flux of a pre-calibrated penray lamp used on the ground based calibration device to $F_\beta$ entering APACHE

Adapted and expanded upon the reasoning:

"Since the pre-characterized ground based calibration device is designed to supply only 50 sL $min^{-1}$, and the sensitivity of airborne HORUS instrument is optimized for high altitude flying, the critical orifice diameter in HORUS was changed from the airborne configuration of 1.4 mm to a 0.8 mm on-ground* configuration. Additionally, the IPI system was switched to passive (i.e. the exhaust line to the IPI blower was capped using a kf 40 flange). This was to adapt HORUS to a mass flow that the ground based calibration device is able to provide and reduces the internal pressure within HORUS (from 18 mbar to 3.5 mbar) to optimize the sensitivity towards OH at ambient ground level pressures (~1000 mbar). The asterisk discerns terms that were quantified when the smaller 0.8 mm critical orifice was used. The calculated instrument on-ground* sensitivity was then used to translate OH and $HO_2$ concentrations produced by the uv-technik Hg ring lamp into a value for $F_\beta$."

439 and 441, another "where" to change

Changed to lower case w

457 and elsewhere, for the units of flux of the light should this be "photons s-1", or even also per unit area?

All flux units have be corrected "photons $cm^{-2}$ $s^{-1}$).

Section 5 is the results, and quite a few are shown, but compared with the rest of the paper this is fairly short, and the discussion ought to be extended a little to fully exploit the results – what behaviour is therefore expected from aircraft measurements based on the lab work?

We have expanded section 5 into section 4. We have also provided additional context and discussion in the section, including instrument behavior during a typical flight.

495. The losses at the inlet were the same for OH and HO2? Some further discussion of this as might expect OH to lost more.

See response 371.

498 "where"

Page 20 – I found this page difficult to follow, there were a lot of losses discussed, quantified by the alpha values, for various stages of the airflow, e.g. the meanings of equations 16-18 and the discussion around this was confusing.

We have expanded on points here and explicitly stated which alpha term is which and how they are summed to together to acquire the total OH and HO2 pressure dependent transmission terms.



522. Remind reader of the two actinometric methods again (as not much detail was give on these two methods earlier).

Removed this paragraph as it did not sit well within the context of the discussion at this point. We talk about the two actinometric methods again within the conclusions.

Section 5.2 seems to be a series of tables 5-8, and a big figure, and there is virtually no text to go with this? Some further discussion is needed to bring this all together, given it is the main results from the paper. From the C factors presented , e.g. in Table 8, can the LOD of the instrument be presented, and this compared with expected levels of OH and HO2 in the atmosphere during the flights?

We have expanded section 5 into section 4. We have also provided additional context and discussion in the section, including instrument behavior during flight. Including LOD.

Figure 10. For the second row on quenching, link this to an equation used in the text – the label of the plot "Overall quenching" is unclear – and some link to the relevant part of the text is needed. Likewise for the other panels. for the first row, the y label is "Overall sensitivity" which I assume is the C(OH) factors etc., and an explicit link should be made. Likewise ALHPA (total) – refer to the equation where that is in the text.

We have included an equation explaining how the quenching is calculated. Within the text and figure explicit links have been included regarding quenching, C(OH), and $ALPHA_{Total}$.

554. The losses of HOx is discussed for the operation of APACHE during the controlled conditions ground testing. Can this be compared with the expected losses during flight when the flow velocity within APACHE may be a somewhat different (or a statement making clear the velocity within APACHE will be the same as here, or similar).

We have included a figure for inflight conditions to allow for discussion and direct comparison, between controlled ground testing and in-flight losses.

566 "is" missing after "system"

Corrected the statement to "However, in this study, the APACHE calibration system has demonstrated that, within the lab, it is sufficiently capable of calibrating the airborne HORUS instrument across the pressure ranges the instrument had experienced in-flight during the OMO-ASIA 2015 airborne campaign."

567 – experienced in flight is mentioned, but make clear again that the tests presented here are on the ground.

See comment above

568. 17-18% overall uncertainty (1 sigma) – explain why this is "suitable" for a calibration approach. Mention is needed of what the measurements will be used for – to compare with OH and HO2 calculations from an atmospheric model – for which there is an uncertainty also – and a robust comparison can only be done if the measurements are accurate to a certain %, etc.

The overall uncertainty is now 22.1 – 22.6 % (1 sigma). We have adjusted this statement to be a direct comparison to the other calibration methods shown in table 1. As of this study we are not addressing an overarching scientific question, and therefore making no statement regarding the "suitability" of this uncertainty.

"The overall uncertainty of 22.1 – 22.6 % (1σ) demonstrates that this calibration approach with APACHE compares well with other calibration methods described earlier in Table 1. Accurate calibrations of instruments, particularly airborne instruments that have strong pressure dependent sensitivities, are critical to acquiring concentrations of atmospheric species with minimal uncertainties. Only through calibrations can the accuracy of measurements be characterized and allow for robust comparisons with other measurements and with models to expand our current understanding of chemistry that occurs within our atmosphere."

The paper focusses on pressure and water vapour, can any comments be made about the expected change in performance (e.g. losses on surfaces, or lamp) with changes in temperature during flights?

The APACHE system is an on ground setup, built to replicate conditions in flight . It is not installed on the aircraft. However, we have highlighted future developments of APACHE to adapt it for temperature control as well as pressure control.

---

Interactive comment on Atmos. Meas. Tech. Discuss., doi:10.5194/amt-2019-439, 2019.

# Calibration of an airborne $HO_X$ instrument using the All Pressure Altitude based Calibrator for $HO_X$ Experimentation (APACHE)

Daniel Marno[1], Cheryl Ernest[1*], Korbinian Hens[1**], Umar Javed[1,2], Thomas Klimach[1], Monica Martinez[1], Markus Rudolf[1], Jos Lelieveld[1], and Hartwig Harder[1]

[1] Atmospheric Chemistry Department, Max Planck Institute for Chemistry, 55128, Mainz, Germany
[2] Forschungszentrum Jülich GmbH, IEK-8, 52425, Jülich, Germany
*now at: Department of Neurology, University Medical Center of the Johannes Gutenberg University Mainz, 55131, Mainz, Germany
**now at: Hübner GmbH & Co KG – Division Hübner Photonics, 34123 Kassel, Germany

**Correspondence:** Daniel Marno (daniel.marno@mpic.de), Hartwig Harder (hartwig.harder@mpic.de)

**Abstract.** Laser induced fluorescence (LIF) is a widely used technique for both laboratory-based and ambient atmospheric chemistry measurements. However, LIF instruments require calibrations in order to translate instrument response into concentrations of chemical species. Calibration of LIF instruments measuring OH and $HO_2$ ($HO_X$), typically involves the photolysis of water vapor by 184.9 nm light thereby producing quantitative amounts of OH and $HO_2$. For ground-based $HO_X$ instruments, this method of calibration is done at one pressure (typically ambient pressure) at the instrument inlet. However, airborne $HO_X$ instruments can experience varying cell pressures, internal residence times, temperatures, and humidity during flight. Therefore, replication of such variances when calibrating in the lab are essential to acquire the appropriate sensitivities. This requirement resulted in the development of the APACHE (All Pressure Altitude-based Calibrator for $HO_X$ Experimentation) chamber, to characterize the sensitivity of the airborne LIF-FAGE $HO_X$ instrument, HORUS, which took part in an intensive airborne campaign, OMO-ASIA 2015. It utilizes photolysis of water vapor, but has the additional ability to alter the pressure at the nozzle of the HORUS instrument. With APACHE, the HORUS instrument sensitivity towards OH (26.1 - 7.8 cts $s^{-1}$ $pptv^{-1}$ $mW^{-1}$, ± 22.6% 1σ) and $HO_2$ (21.2 - 8.1 cts $s^{-1}$ $pptv^{-1}$ $mW^{-1}$, ± 22.1% 1σ) was characterized to the external pressure range at the instrument nozzle of 227 - 900 mbar. Measurements supported by a computational fluid dynamics model, COMSOL multiphysics, revealed that, for all pressures explored in this study, APACHE is capable of initializing homogenous flow and maintaining near uniform flow speeds across the internal cross-section of the chamber. This reduces the uncertainty regarding average exposure times across the mercury (Hg) UV ring lamp. Two different actinometrical approaches characterized the APACHE UV ring lamp flux as 6.37 x $10^{14}$ (± 1.3 x $10^{14}$) photons $cm^{-2}$ $s^{-1}$. One approach used the HORUS instrument as a transfer standard in conjunction with a calibrated on-ground calibration system traceable to NIST standards, which characterized the UV ring lamp flux to be 6.9 (± 1.1) x$10^{14}$ photons $cm^{-2}$ $s^{-1}$. The second approach involved measuring ozone production by the UV ring lamp using an ANSYCO O3 41 M ozone monitor, which characterized the UV ring lamp flux to be 6.11 (± 0.8) x$10^{14}$ photons $cm^{-2}$ $s^{-1}$. Data presented in this study are the first direct calibrations of an airborne $HO_X$ instrument, performed in a controlled environment in the lab using APACHE.

## 1 Introduction

It is well known that the hydroxyl (OH) radical is a potent oxidizing agent in daytime photochemical degradation of pollutants sourced from anthropogenic and biogenic processes thus accelerating their removal from our atmosphere. The hydroperoxyl radical ($HO_2$) also

**Formatiert:** Block
**Gelöscht:** systems
**Gelöscht:** .
**Gelöscht:** inlet
**Gelöscht:** $HO_X$
**Gelöscht:** thus relating
**Gelöscht:** to
**Gelöscht:** s
**Gelöscht:**
**Gelöscht:** experienced during flight
**Gelöscht:** (
**Gelöscht:** 5
**Gelöscht:** to
**Gelöscht:** 1000
**Gelöscht:** )
**Gelöscht:** COMSOL multiphysics and its
**Gelöscht:** calculations
**Gelöscht:** 3
**Gelöscht:** 0.9
**Gelöscht:** depending on pressure.
**Gelöscht:** in a
**Gelöscht:** of an airborne $HO_X$ system instrument
**Gelöscht:** ¶

plays a central role in atmospheric oxidation as it not only acts as a reservoir for OH, but is involved in formation of other oxidants such as peroxides and impacts the cycling of pollutants such as $NO_X$ (= NO + $NO_2$) (Lelieveld et al., 2002). Therefore, measurements of OH and $HO_2$ ($HO_X$) within the troposphere are essential in understanding the potential global scale impacts of pollutants in both the present day and in climate predictions. One common $HO_X$ measurement method is Laser Induced Fluorescence (LIF) (Stevens et al., 1994; Brune et al., 1995; Hard et al., 1995; Martinez et al., 2003; Faloona et al., 2004; Stone et al., 2010; Hens et al., 2014; Novelli et al., 2014). Other methods have been successfully implemented to measure $HO_X$. Chemical Ionization Mass Spectrometry (CIMS) (Cantrell et al., 2003; Mauldin et al., 2004; Sjostedt et al., 2007; Dusanter et al., 2008; Kukui et al., 2008; Albrecht et al., 2019) and Differential Optical Absorption Spectroscopy (DOAS) (Brauers et al., 1996; Brauers et al., 2001; Schlosser et al., 2007) have also been used in the measurement of $HO_X$ in the field and in intercomparison projects with LIF instrumentation. However, low atmospheric concentrations of $HO_X$ (Schlosser et al., 2009) and potential interferences (Faloona et al., 2004; Fuchs et al., 2011; Mao et al., 2012; Hens et al., 2014; Novelli et al., 2014; Fuchs et al., 2016) can make $HO_X$ measurements especially challenging. Airborne LIF-FAGE (LIF-Fluorescence Assay by Gas Expansion) instruments experience large variability in pressure, humidity, instrument internal air density, and internal quenching during flights, which cause a wide array of instrumental sensitivities (Faloona et al., 2004; Martinez et al., 2010; Regelin et al., 2013; Winiberg et al., 2015). Therefore, it is critical to utilize a calibration system that can suitably reproduce in-flight conditions to determine the instrument response to known levels of OH and $HO_2$ to acquire robust $HO_X$ measurements.

The first stage of the Hydroxyl Radical measurement Unit based on fluorescence Spectroscopy (HORUS) inlet is an inlet pre-injector (IPI), used to determine the concentration of background OH interferences by removing atmospheric OH from the signal via addition of an OH scavenger such as propane. IPI draws 50-230 sL $min^{-1}$ depending on altitude and is susceptible to temperature and pressure-driven changes in internal reaction rates and residence times under flight conditions. This has implications for the removal of atmospheric OH in the inlet and for the characterization of background interference signals in HORUS. Therefore, a device capable of providing stable high flows whilst reproducing a wide range of pressures and temperatures is needed in order to calibrate the airborne HORUS instrument. This led to the production, characterization, and utilization of the calibration device APACHE (All Pressure Altitude based Calibrator for $HO_X$ Experimentation) which is described in depth in this work.

## 2 Experimental design and set up

### 2.1 APACHE design overview

Figure 1 shows the overview of the APACHE system. In front of the APACHE inlet, a series of mixing blocks are installed where multiple dry synthetic air additions are injected into a controlled humidified air supply ensuring thorough mixing of water vapor before being measured by a LI-COR 6262 $CO_2$/$H_2O$ (Figure 1a). This air is then fed into a large mass flow controller (MFC). The construction of the APACHE chamber itself is shown in Figure 1b. The first section contains the diffuser inlet with a sintered filter (bronze alloy, Amtag, filter class 10). This 2 mm thick sintered filter, with a pore size of 35 µm, initializes a homogeneous flow and further improves the mixing of water vapor in front of the UV ring lamp (described further in section 4). The water photolysis section contains a low-pressure, 0.8 A, mercury ring lamp (uv-technik, see supplementary, Figure S.1) which produces a constant radial photon flux at

**Gelöscht:** However,
**Gelöscht:** o
**Gelöscht:** our
**Gelöscht:** .
**Gelöscht:** were
**Gelöscht:** were
**Gelöscht:** figure
**Gelöscht:** figure
**Gelöscht:** which
**Gelöscht:** before passing over
**Gelöscht:** figure

184.9 nm, situated 133 mm after the sintered filter and separated from the main APACHE chamber by an airtight quartz window. Between the lamp and the quartz window there is an anodized aluminum band with thirty 8 mm apertures blocking all light apart from that going through the apertures, which reduces the amount of UV flux entering APACHE and limits the

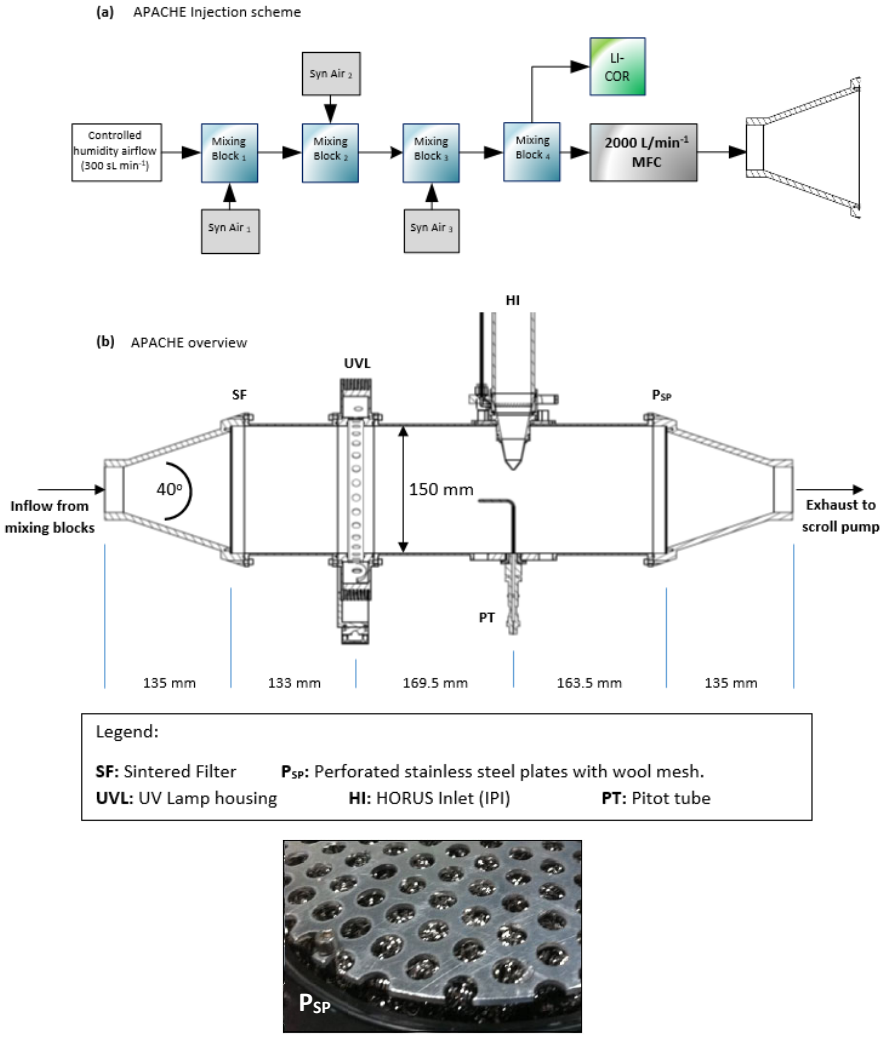


**Figure 1.** Overview of the APACHE system and the pre-mixing set up used in the lab to calibrate the HORUS airborne instrument. A picture at the bottom shows the perforated stainless steel plates with wool mesh.

size of the illuminated area. The IPI system is clamped down 169.5 mm behind the photolysis section in such a way that the instrument sample flow is perpendicular to the airflow passing over the IPI nozzle. The nozzle protrudes 51.5 mm into the APACHE cavity much like it is when installed in the aircraft shroud system (see Figure 2), and is made air tight with the use

**Gelöscht:**

**Gelöscht:** , which blocks

**Gelöscht:** controls

**Formatiert:** Block

**Gelöscht:** HORUS inlet

**Gelöscht:** after

**Gelöscht:** inlet

**Gelöscht:** inlet

**Gelöscht:** figure

of O-rings. Opposite the IPI nozzle, there is an airtight block attachment containing a series of monitoring systems. A pitot tube attached to an Airflow PTSX-K 0-10Pa differential pressure sensor (accuracy rating of 1% at full scale, 1σ) is used to monitor the internal flow speeds within APACHE. A 3 kOhm NTC-EC95302V thermistor is used to monitor the air temperature and an Edwards ASG2-1000 pressure sensor (with an accuracy rating of ± 4 mbar, 2σ) monitors the static air pressure. Additionally, there are two one-quarter inch airtight apertures in the monitoring block that can be opened to enable other instrumentation to be installed.

## 2.2 Pressure control

For this study, the operational pressure range of APACHE used was 227 – 900 mbar, with precision of ± 0.1% (1σ) and accuracy of ± 2% (1σ) with mass flows ranging from 200 to 990 sL min$^{-1}$. This was achieved using an Edwards GSX160 scroll pump controlling the volume flow in combination with a MFC (Bronkhorst F-601A1-PAD-03-V) controlling the mass flow of air entering APACHE. This system reached air speeds of 0.9 to 1.5 m s$^{-1}$ through APACHE at pressures ranging from 250 to 900 mbar and at temperatures ranging from 282 to 302 K. Temperature changes inside APACHE are not controlled. However, as air temperature is measured throughout the calibration device and HORUS, any term that is affected by temperature is characterized using the corresponding measured temperature values. Although not critical for this study, the operational pressure range of APACHE can be extended by changing the draw speed of the Edwards scroll pump. However, that may cause the flow speeds and potentially the flow speed profiles across the UV ring lamp to vary in between different pressure calibrations.

## 2.3 The airborne HORUS instrument

The LIF-FAGE instrument developed by our group (HORUS), is based on the original design of GTHOS (Ground Tropospheric Hydrogen Oxide Sensor) described by Faloona et al. (2004) and is described in further detail by Martinez et al. (2010). The airborne instrument is a revised and altered design to perform under conditions experienced during flight and conform to aeronautical regulations. It was primarily developed for installation on the High Altitude and Long Range Research Aircraft (HALO) and took place in the OMO-Asia 2015 airborne campaign. The system comprises of an external inlet shroud, detections axes, laser system, and a vacuum system (Figure. 2). Additionally, this is the first airborne LIF-FAGE instrument measuring $HO_X$ with a dedicated inlet pre injector (IPI) system installed for the purpose of removing atmospheric OH enabling real time measurements and quantification of potential chemical background OH interferences, OH-CHEM (Mao et al., 2012). The airborne IPI system is redesigned to fit within the shroud inlet system and its walls are heated to 30 °C, whilst maintaining similar operational features as the on-ground IPI installation (Novelli et al., 2014). To prevent excessive collisions of OH and $HO_2$ with the IPI nozzle and internal walls, thus limiting losses of $HO_X$ during flight, the momentum inertia of the air passing through the external shroud system had to be overcome to promote flow direction into the instrument. This was achieved by installing a choke point behind the IPI nozzle in the inlet shroud, resulting in a reduction in air flow speed. For example without the shroud choke, flow speeds in excess of 200 m s$^{-1}$ could occur in the shroud during flight. However, with the choke point, flow speeds in the shroud during flight did not exceed 21 m s$^{-1}$ during OMO-Asia 2015, which is sufficiently below the sample velocities of IPI during flight (44 – 53 m s$^{-1}$). Additionally, it limits non-parallel flows across the IPI nozzle created by variable pitch, roll and yaw changes of the aircraft. As the aircraft changes pitch, roll and yaw, the measured OH variability increases by ± 4.51 x10$^{4}$ cm$^{-3}$ (1σ), which is only 10 to 15 % higher than the natural variability of OH. This

**Gelöscht:** HORUS inlet

**Gelöscht:** ¶
¶
One system being a

**Gelöscht:** , which

**Gelöscht:** ¶

**Formatiert:** Einzug: Erste Zeile: 0,5 cm

**Gelöscht:** 250

**Gelöscht:** This was achieved by an Edwards GSX160 scroll pump controlling the volume flow, which resulted in air speeds of 0.9 to 1.5 m s$^{-1}$ through APACHE at 250 and 1000 mbar respectively at 25 °C, used in combination with a MFC (Bronkhorst F-601A1-PAD-03-V) capable of controlling a mass flow of up to 2000 sL min$^{-1}$ dictating the mass flow of air entering APACHE and thus controlling the pressure.

**Gelöscht:** figure

**Gelöscht:** ¶
¶

**Gelöscht:** orifice

**Gelöscht:** in the shroud

**Gelöscht:** instrument inlet

**Gelöscht:** to decrease

**Gelöscht:**

**Gelöscht:** from

**Gelöscht:** ~

**Gelöscht:**

**Gelöscht:** to <

**Gelöscht:** y

**Gelöscht:** HORUS

**Gelöscht:** HORUS inlet

**Gelöscht:** on average

increase in variability is negligible as is represents, depending on internal pressure, 19 to 30 % of the detection limit of the instrument. Both these effects of the external shroud improve the measurement performance by reducing variable wall losses of $HO_X$ at the IPI nozzle under flight conditions. The IPI system (with a nozzle orifice diameter of 6.5 mm) samples (51 to 230 sL $min^{-1}$) from the central air flow moving through the internal shroud. A critical orifice is located at the end of IPI in the center of the IPI cross section, which enables the HORUS instrument to sample (3 to 17 sL $min^{-1}$) from the central flow moving through IPI. This further reduces influences of wall loss within IPI on the overall measured signal in the cells. The removal of excess flow moving through IPI occurs via a perforated ring that surrounds the base of the critical orifice cone, evacuated by a blower.

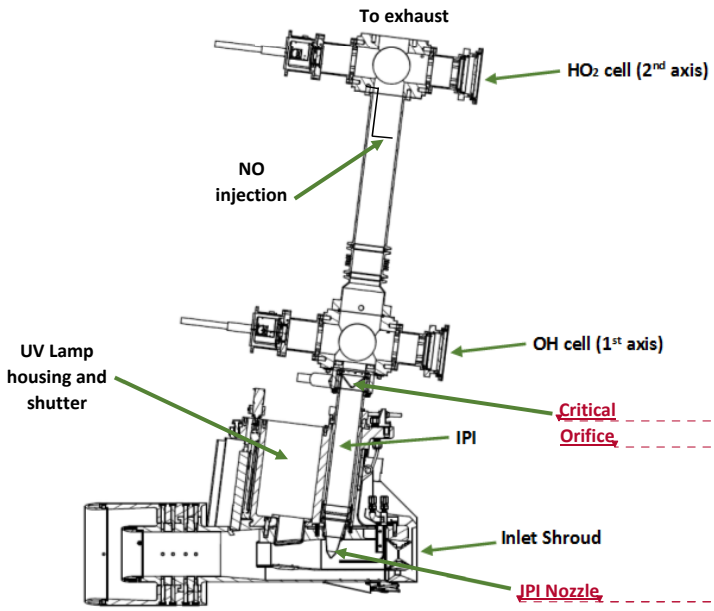


**Figure 2.** Overview of the airborne HORUS system as installed in the HALO aircraft. $HO_2$ is measured indirectly through the addition of NO that quantitatively converts $HO_2$ into OH. The NO injection occurs via a stainless steel 1/8 inch line, shaped into a ring perpendicular to the airflow with several unidirectional apertures of 0.25 mm diameter creating essentially a NO shower.

As with other LIF-FAGE $HO_X$ instruments, HORUS measures an off-resonance signal to discern the net OH fluorescence signal. This is achieved by successive cycling of the laser tuning from on-resonance (measuring the total signal of OH fluorescence and the signal originating from other fluorescence and electronic sources), to off-resonance (measuring all the above except the OH fluorescence). The HORUS instrument utilizes the $Q_1(2)$ transition $X^2\Pi_{3/2}(v'' = 0) \rightarrow A^2\Sigma^+(v' = 0)$ (Freeman. 1958; Dieke and Crosswhite. 1962; Langhoff et al., 1982; Dorn et al., 1995; Holland et al., 1995; Mather et al., 1997). The net OH signal ($S_{OH}$) is the difference between the on-resonance and off-resonance signals, OH-WAVE (Mao et al., 2012). The OH sensitivity ($C_{OH}$) and average laser power within the detection axis ($Wz_{1\ pwr}$) are then used to calculate the absolute OH mixing ratio (see Eq. (1)). $HO_2$ is measured indirectly

**Gelöscht:** HORUS inlet

**Formatiert:** Schriftart: (Standard) Times New Roman, 12 Pt., Schriftfarbe: Automatisch

**Formatiert:** Schriftart: (Standard) Times New Roman, 12 Pt., Schriftfarbe: Automatisch

**Formatiert:** Schriftart: (Standard) Times New Roman, 12 Pt., Schriftfarbe: Automatisch

**Gelöscht:** NO

**Gelöscht:** injection

**Gelöscht:** NO

**Gelöscht:** injection

**Gelöscht:** ¶

**Gelöscht:** ¶
¶
¶
¶

**Formatiert:** Schriftart: (Standard) +Textkörper (Calibri), 11 Pt., Englisch (Vereinigtes Königreich)

**Formatiert:** Deutsch (Deutschland)

**Formatiert:** Deutsch (Deutschland)

**Gelöscht:** thus

through the quantitative conversion of atmospheric $HO_2$ to OH by injection of nitric oxide (NO) under the low-pressure conditions within HORUS.

$$HO_2 + NO \rightarrow NO_2 + OH \qquad (R1)$$

When NO is injected into the instrument, both ambient OH and $HO_2$ are measured in the second detection axis. The net $HO_2$ signal ($S_{HO2}$) in the second axis is therefore derived from subtracting the net OH signal from the first detection axis normalized by the ratio of the OH sensitivities for the two detection axes ($C_{OH(2)}$ / $C_{OH}$) from the net $HO_X$ signal ($S_{HOx}$). Then $S_{HO2}$ is corrected by the sensitivity to $HO_2$ ($C_{HO2}$) and laser power ($Wz_{2\,pwr}$) to reach absolute $HO_2$ mixing ratio (see Eq. (2)).

$$[OH] = \frac{S_{OH}}{(C_{OH} \cdot Wz_{1\,pwr})} \qquad (1)$$

$$[HO_2] = \frac{1}{(C_{HO_2} \cdot Wz_{2\,pwr})} \cdot \left\{ S_{HO_X} - \frac{(C_{OH(2)} \cdot Wz_{2\,pwr})}{(C_{OH} \cdot Wz_{1\,pwr})} S_{OH} \right\} \qquad (2)$$

where, $Wz_{1\,pwr}$ is the laser power in the first detection axis, $Wz_{2\,pwr}$ is the laser power in the second detection axis and $C_{OH}$ and $C_{HO2}$ are the calibrated sensitivity factors for OH and $HO_2$ (cts $s^{-1}$ $pptv^{-1}$ $mW^{-1}$) respectively. By calibrating using a known OH mixing ratio, the instrument sensitivity $C_{OH}$ can be determined by rearranging Eq. (1) to:

$$C_{OH\,(cal)} = {S_{OH_{cal}}}/{([OH] \cdot Wz_{1\,pwr})} \qquad (3)$$

The sensitivity of HORUS depends on the internal pressure, water vapor mixing ratios, and temperature, which are subject to change quite significantly during flight. Therefore, further parameterization when calibrating is required to fully constrain the sensitivity response of the instrument at various flight conditions. Eq. (4) shows the terms that affect the sensitivity of the first HORUS axis that measures OH.

$$C_{OH}(P,T) = c0 \cdot \rho_{Int}(P,T) \cdot Q_{IF}(P,T,H_2O) \cdot b_c(T) \cdot [\alpha_{IPI}(P,T) \cdot \alpha_{HORUS}(P,T)] \qquad (4)$$

where c0 is determined by calibrations and is the lump sum coefficient of all the pressure independent factors affecting the HORUS sensitivity, for example, OH absorption cross section at 308nm, the photon collection efficiency of the optical setup and quantum yield of the detectors, as well as pressure independent wall loss effects. For calibrations, c0 is normalized by laser power and has the units (cts $pptv^{-1}$ $s^{-2}$ $cm^3$ $molecule^{-1}$ $mW^{-1}$). $\rho_{Int}$ is the internal molecular density. $Q_{IF}$ is the quenching effect (s), which consists of the natural decay frequency of OH, OH decay due to collisional quenching that is dependent on pressure, temperature, and water vapor mixing ratio, and the detector opening and closing gating times after the initial excitation laser pulse. Both are pressure dependent terms as denoted in Eq. (4). The Boltzmann correction ($b_c$) has a temperature dependency as it corrects for any OH molecules that enter the HORUS instrument in a thermally excited state and are therefore not measurable by fluorescence excitation at the wavelength used. α is the pressure dependent OH transmission, which is the fraction of OH that reaches the point of detection. This term is separated for the two-tier pressure conditions present in the instrument. The term $\alpha_{IPI}$ represents the correction for pressure and temperature dependent OH loss on the walls within IPI. The term $\alpha_{HORUS}$ is the correction for pressure dependent OH loss to the walls within the HORUS detection axes post critical orifice. Whilst the quenching effects, internal densities and Boltzmann corrections

**Gelöscht:** ¶

**Formatiert:** Einzug: Erste Zeile: 0 cm

**Gelöscht:** OH

**Gelöscht:** ¶

**Formatiert:** Einzug: Erste Zeile: 0 cm

**Gelöscht:** $HO_2$

**Gelöscht:** $\left\{S_{HO_X} - \frac{C_{OH(2)}}{C_{OH}} S_{OH}\right\}$

**Gelöscht:**

**Gelöscht:** OH

**Gelöscht:**

**Gelöscht:** $\cdot\ Wz_{pwr}$

**Gelöscht:**

**Gelöscht:** Where

**Formatiert:** Einzug: Erste Zeile: 0 cm

**Gelöscht:** (cts $cm^3$ $molecule^{-1}$ $s^{-1}$)

**Gelöscht:** of $N_2$, $O_2$ and $H_2O$ occurring inside the detection axis, which is normalized to 1 % water mixing ratio

**Gelöscht:** $Wz_{pwr}$ is the measured laser power entering the white cell in the detection axis.

**Gelöscht:** (post pinhole, pre-critical orifice)

can be quantified by calculation, and the power entering the measurement cell is measured, the two factors that need to be determined through calibration are c0 and OH transmission, α. Once the c0 coefficient and α terms are known, the final in-flight measured OH mixing ratio (pptv) is found:

$$[OH] = {S_{OH}}/{(c0 \cdot \rho_{Int} \cdot Q_{IF} \cdot b_c \cdot [\alpha_{IPI} \cdot \alpha_{HORUS}] \cdot Wz_{1\,pwr})} \quad (5)$$

As $S_{OH}$ scales with laser power, the terms that describe the instrument sensitivity shown as the denominator in Eq. (5), which ultimately have the units cts $s^{-1}$ $pptv^{-1}$ $mW^{-1}$, must also be scaled to the measured laser power ($Wz_{1\,pwr}$) during flight to acquire the absolute measurement of OH mixing ratio. As depicted in both Figure 1b and Figure 2, the complete system is calibrated with IPI attached and operating as it did when installed in the aircraft. Therefore, the combined losses of OH within IPI and in the low pressure regime post critical orifice (that has a diameter of 1.4 mm) contribute to the overall calibrated $C_{OH}$ sensitivity factor in the same way during measurement and calibrations, meaning that the OH transmission of HORUS can be quantified with both OH transmission terms ($\alpha_{IPI}$ and $\alpha_{HORUS}$) combined into one term ($\alpha_{Total}$).

$$[OH] = {S_{OH}}/{(c0 \cdot \rho_{Int} \cdot Q_{IF} \cdot b_c \cdot [\alpha_{Total}] \cdot Wz_{1\,pwr})} \quad (6)$$

Figure 3 shows the schematic of the different factors described above and their impact on the overall sensitivity.

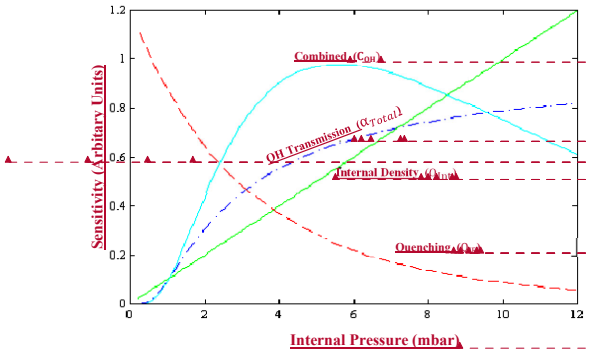


**Figure 3.** A schematic showing the overall sensitivity curve as a function of internal pressure (light blue line), OH transmission (dotted-dashed dark blue line), internal density (green line), and the quenching (dashed red line).

## 3 Calibration method and theory

As an overview, Table 1 shows common calibration techniques for OH instruments. The APACHE system is based on the production of known quantified and equal concentrations of OH and $HO_2$ via photolysis of water vapor in only synthetic air using a Hg ring lamp emitting UV radiation at 184.9 nm.

$$H_2O + h\upsilon \xrightarrow{\lambda=184.9\,nm} OH + H^* \quad (R2)$$

$$H^* + O_2 \xrightarrow{O_2} OH + O_3 \quad (R3)$$

Formatiert ... [1]
Gelöscht: OH
Gelöscht: · $Wz_{pwr}$
Gelöscht: ·
Gelöscht:
Gelöscht: figure
Gelöscht: figure
Gelöscht: OH
Gelöscht: · $Wz_{pwr}$
Gelöscht:
Gelöscht: graphical representation
Formatiert ... [22]
Formatiert ... [23]
Formatiert ... [24]
Formatiert ... [17]
Formatiert ... [16]
Formatiert ... [18]
Formatiert ... [19]
Formatiert ... [20]
Formatiert ... [21]
Formatiert ... [4]
Formatiert ... [5]
Formatiert ... [6]
Formatiert ... [7]
Formatiert ... [8]
Formatiert ... [9]
Formatiert ... [10]
Formatiert ... [11]
Formatiert ... [12]
Formatiert ... [13]
Formatiert ... [14]
Formatiert ... [15]
Formatiert ... [25]
Formatiert ... [26]
Formatiert ... [27]
Formatiert ... [28]
Formatiert ... [29]
Formatiert ... [30]
Formatiert ... [31]
Formatiert ... [32]
Formatiert ... [3]
Gelöscht: ¶
Formatiert ... [2]
Gelöscht: table
Gelöscht: pure

$$H^* \xrightarrow{M} H \quad \text{(R4)}$$

$$H + O_2 \xrightarrow{M} HO_2 \quad \text{(R5)}$$

**Table 1.** Various known methods for OH instrument calibrations

| | Technique | Method | Quoted (1σ) Uncertainty | Limitations | References |
|---|---|---|---|---|---|
| (I) | Water UV-Photolysis | See sections 3 and 4 | 10-30% | Dependent on lamp, photon flux measurement, and absorption | (Creasey et al., 2003; Heard and Pilling. 2003; Holland et al., 2003; Ren et al., 2003; Faloona et al., 2004; Smith et al., 2006; Martinez et al., 2010; Mallik et al., 2018) |
| (II) | Pulsed $N_2$-$H_2O$ RF discharge | At low pressure (0.1 Torr); OH and NO produced using a low power RF discharge. Concentrations of NO and OH are closely linked | 20% | Requires NO measurement using stable ambient air calibrations | (Dilecce et al., 2004; Verreycken and Bruggeman. 2014) |
| (III) | Low-pressure flow-tube RF discharge | OH radical production by titration of H atoms with $NO_2$. Known amount of H atoms produced using microwave discharge using low pressure flow tube | 30% | Stable ambient air calibrations | (Stevens et al., 1994) |
| (IV) | Continuously Stirred Tank Reactor and decay of select hydrocarbons | In a CSTR, OH produced through UV-irradiation of humidified air flow with injection of a specific Hydrocarbon (1,3,5-trimethylbenzene, $C_9H_{12}$) and NO. More recent studies have used Cyclohexane, n-pentane and iso-butene Concentrations of OH relates to decay rate of the Hydrocarbon | 24-36% | Time intensive, systematic wall loss of OH in reactor | (Hard et al., 1995; Hard et al., 2002; Winiberg et al., 2015) |
| (V) | Steady-State $O_3$-alkene | A steady state OH concentration produced from ozonolysis of a known concentration of an alkene | 42% | Time consuming, large uncertainties compared to other methods | (Heard and Pilling. 2003; Dusanter et al., 2008) |
| (VI) | Laser photolysis of Ozone | Photolysis of $O_3$ with 284 nm light producing $O(^1D)$. Which then reacts with $H_2O$ producing OH | 40-50% | Requires large apparatus | (Tanner and Eisele. 1995) |

Stable water mixing ratios with a variability of < 2 % were achieved by heating 300 sL min$^{-1}$ flow of synthetic air to 353 K and introducing deionized water using a peristaltic pump into this heated gas flow causing it to evaporate before entering a 15 L mixing chamber. This prevents re-condensation and humidity spikes when the pump is introducing the water. The

**[2] nach unten verschoben:** Stable water mixing ratios with a variability of < 2 % were achieved by heating 300 sL min$^{-1}$ flow of synthetic air to 353 K and introducing deionized water using a peristaltic pump into this heated gas flow causing it to evaporate before entering a 15 L mixing chamber. This prevents re-condensation and humidity spikes when the pump is introducing the water. The humidified gas flow is then diluted (to around 3 mmol mol$^{-1}$) and mixed further with additional dry pure synthetic air via a series of mixing blocks to achieve the required and desired stable water vapor mixing ratios. The photolysis of $H_2O$ has only one spin-allowed and energetically viable dissociation channel at 184.9 nm (Engel et al., 1992), meaning the quantum yield of OH and H* are unified (Sander et al., 2003). Even though reaction R3 is possible particularly since the H* atoms can carry transitional energies of 0.7 eV at 189.4nm (Zhang et al., 2000), the fast removal of energy by reaction R4 allows for the general assumption that all H * atoms produced leads to $HO_2$ production. The use of water photolysis as a OH and $HO_2$ radical source for calibration of $HO_X$ instruments has been adopted in a number of studies (Heard and Pilling. 2003; Ren et al., 2003; Faloona et al., 2004; Dusanter et al., 2008; Novelli et al., 2014; Mallik et al., 2018). As an example, the factors required to quantify the known concentrations of OH and $HO_2$ during calibrations are shown below:¶

**Gelöscht:** $[OH] = [HO_2] = [H_2O] \cdot \sigma_{H_2O} \cdot F_{184.9\,nm}$ ... [34]

**Gelöscht: Table 1.** Various known methods for OH instrument calibrations.¶ ... [35]

**Formatiert** ... [33]

**Formatierte Tabelle**

**Gelöscht:** ¶
Technique ... [36]

**Formatiert:** Block

**Formatiert:** Block

**Formatiert:** Block

**Formatiert:** Block

**Formatiert:** Block

**Formatiert:** Block

**Formatiert:** Block

**Formatiert:** Block

**Formatiert:** Block

**Formatiert:** Block

**Formatiert:** Block

**Formatiert:** Block

**Formatiert:** Block

**Formatiert:** Block

**Formatiert:** Block

**Gelöscht:** ¶

**[2] verschoben (Einfügung)**

humidified gas flow is then diluted (to around 3 mmol mol$^{-1}$) and mixed further with additional dry pure synthetic air via a series of mixing blocks to achieve the required and desired stable water vapor mixing ratios. The photolysis of $H_2O$ has only one spin-allowed and energetically viable dissociation channel at 184.9 nm (Engel et al., 1992), meaning the quantum yield of OH and H* are unified (Sander et al., 2003). Even though reaction R3 is possible particularly since the H* atoms can carry transitional energies of 0.7 eV at 189.4nm (Zhang et al., 2000), the fast removal of energy by reaction R4 allows for the general assumption that all H * atoms produced leads to $HO_2$ production (Fuchs et al., 2011). The use of water photolysis as a OH and $HO_2$ radical source for calibration of $HO_X$ instruments has been adopted in a number of studies (Heard and Pilling. 2003; Ren et al., 2003; Faloona et al., 2004; Dusanter et al., 2008; Novelli et al., 2014; Mallik et al., 2018). As an example, the factors required to quantify the known concentrations of OH and $HO_2$ during calibrations are shown below:

$$[OH] = [HO_2] = [H_2O] \cdot \sigma_{H_2O} \cdot F_{184.9\,nm} \cdot \phi_{H_2O} \cdot t \qquad (7)$$

where in Eq. (7), the OH and $HO_2$ concentrations are a product of photolysis of a known concentration of water vapor [$H_2O$], $\sigma_{H2O}$ is the absorption cross section of water vapor, 7.22 (± 0.22) x $10^{-20}$ cm$^2$ molecule$^{-1}$ at 184.9 nm (Hofzumahaus et al., 1997; Creasey et al., 2000). $F_{184.9\,nm}$ is the actinic flux (photons cm$^{-2}$ s$^{-1}$) of the mercury lamp used for photolysis, $\phi_{H2O}$ is the quantum yield and t is exposure time. The quantum yield of water vapor photolysis at the 184.9 nm band is 1 (Creasey et al., 2000).

# 4 Results and Discussion

## 4.1 Flow conditions

With any calibration device, the flow conditions must be characterized to inform subsequent methods and calibrations. Regarding APACHE, the two main factors to be resolved are (i) how uniform are the flow speed profiles and therefore exposure times in respect to the APACHE cross section, and (ii) the impact of OH wall losses.

To this end, experimental and model tests were performed to determine whether the combination of the sintered filter, and the stainless steel perforated plates and wool arrangement could provide a homogeneous flow. This means that under operation the flow speeds should be uniform along the cross section of APACHE to within the uncertainty of the measurements. This is to ensure that the air masses passing across the lamp have the same exposure times irrespective of where they are in the cross section. Additionally, model simulations can provide an indication of, as a function of APACHE pressure, the development and scale of boundary air conditions where air parcels experience extended contact time with the interior walls of APACHE, and so have pronounced OH wall losses. This highlights potential flow conditions where there is sufficient time between the photolysis zone and the IPI nozzle to allow APACHE boundary air to expand into and influence the OH content of the air being sampled by HORUS.

### 4.1.1 Flow speed profiles

During calibration, the pressures within the HORUS instrument had to be controlled and monitored to replicate the in-flight conditions. The APACHE chamber pressure is equivalent to the in-flight pressure in the shroud where the HORUS system samples. The pressure of the detection axes depends on the pressure at the IPI nozzle and the efficiency of the pumps. Within

**Feldfunktion geändert**

**Feldfunktion geändert**

**Gelöscht:** W

**Gelöscht:** ¶

**Gelöscht:** APACHE conditions and parametrizations

**Gelöscht:** HORUS inlet

**Gelöscht:** ¶

**Formatiert:** Einzug: Erste Zeile: 0 cm

**Gelöscht:** ¶

**Formatiert:** Einzug: Erste Zeile: 0,63 cm

**Gelöscht:** During calibration, the pressures within the HORUS instrument had to be controlled and monitored to replicate the inflight conditions. The APACHE chamber pressure is equivalent to the inflight pressure in the shroud where the

**Gelöscht:** inlet

**Gelöscht:** For

IPI itself, the airflow through it is dependent on the pressure gradient between the shroud and the ambient pressure at the IPI exhaust or alternatively the APACHE pressure and pressure in front of the XDS 35 scroll pump (post IPI blower). During the campaign, the exhausts of all blowers and pumps of the HORUS system were attached to the passive exhaust system of the aircraft and were thus exposed to ambient pressure. Therefore, the same IPI blower and pumps that were installed on HALO were used in the lab, and throughout the calibrations the pressure at the exhaust for every blower and pumps involved in the HORUS instrument was matched to the respective in-flight ambient pressures by attaching a separate pressure sensor, needle valve and XDS35 scroll pump system. Additionally, to match the power that is provided on the aircraft, a 3-phase mission power supply unit was used to power the pumps in the lab during testing and throughout the calibrations. Figure 4 shows the lab setup described above.

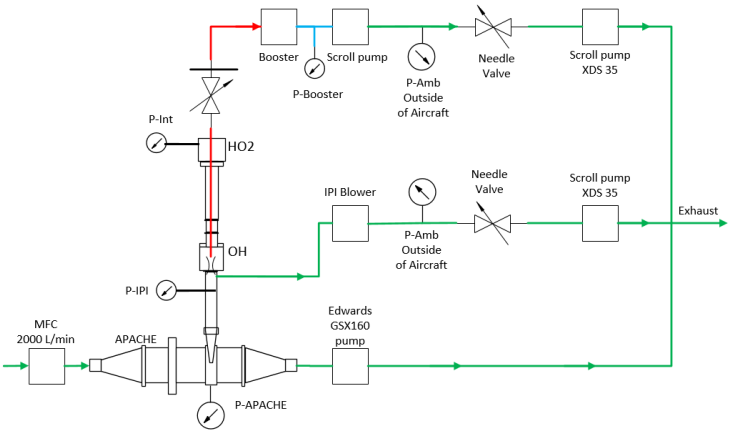


**Figure 4.** The experimental setup with the additional needle valves, pressure sensors and XDS35 scroll pumps attached to the exhausts of all pumps and blowers of HORUS to match in-flight pumping efficiencies when calibrating with APACHE. The red lines depict the low-pressure region within HORUS, the blue is the pressure monitoring line between the booster and scroll pump that drive the HORUS sample flow, and the green show the external gas lines.

To limit the effect of wall loss, HORUS samples air from the core of the APACHE flow system and draws only a fraction of the total air flow as shown in Figure 5. At 900 hPa the HORUS instrument takes 20 % and at 275 hPa HORUS takes 30 % of the total volume flow entering APACHE. To validate that this proportional volume flow into HORUS does not disturb the flow conditions within APACHE, flow speed profiles were performed using the Prandtl pitot tube installed directly opposite the IPI nozzle, which can be positioned flush against the internal wall up to 60.5 mm into the APACHE cavity, which is 15 mm from the APACHE center. Figure 6 shows the measured flow speed profile (blue data points) when the APACHE pressure was 920 hPa. As the distance between the APACHE wall and the pitot tube inlet increased, no significant change in the flow speed was observed. The largest change observed was between 46.6 and 60.5 mm where the flow speed increased by 0.16 m $s^{-1}$, which is 22.8 % smaller than the combined uncertainty of these two measurements ± 0.21m $s^{-1}$ (2σ). Compared to the other four measurement points performed at 920 mbar, the 1.54 m $s^{-1}$ measured at 60.5 mm is not significantly different. However, when performing the speed profile tests at lower pressures, the pressure difference measured was close to or below the

**Gelöscht:** however

**Gelöscht:** ,

**Gelöscht:** for

**Gelöscht:** every

**Gelöscht:** ¶
¶
¶

**Gelöscht:** figure

**Gelöscht:** HORUS inlet

**Gelöscht:** *<Objekt>*

**Gelöscht:**

**Gelöscht:** the low

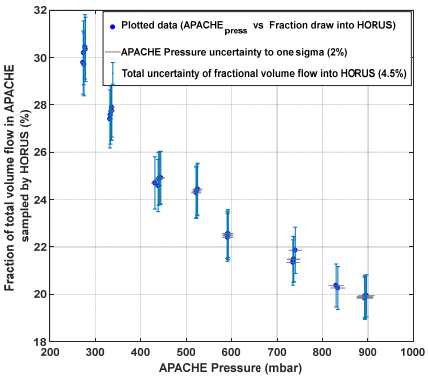


**Figure 5.** The percentage of the total volume flow entering APACHE, which is sampled by HORUS as a function of pressure within APACHE. All error bars are quoted to 1σ.

resolution of the differential pressure sensor. Consequently, the flow inside APACHE and the JPI nozzle was simulated using the computational fluid dynamics (CFD) model from COMSOL multiphysics to gain a better understanding of the flow speed profiles at all pressures. The CFD module in COMSOL uses Reynolds Averaged Navier-Stokes (RANS) models (COMSOL. 2019). The standard k-epsilon turbulence model with incompressible flows was used for this study as it is applicable when investigating flow speeds below 115 m $s^{-1}$ (COMSOL. 2019). An extra fine gridded mesh of a perforated plate with a high solidity ($\sigma_s$ = 0.96) was implemented in the turbulence model to generate the turbulence and replicate the flows created by the bronze sintered filter (Roach. 1987). The model was constrained with the pressures measured within APACHE and JPI. The volume flow was calculated from the measured mass flow entering APACHE and temperatures were constrained using the thermistor readings. To gain confidence in the model, the flow speed output data was compared to the available measured flow speed profile, see Figure 6.

**Formatiert:** Einzug: Erste Zeile: 0 cm

**Gelöscht:** HORUS inlet

**Gelöscht:** system

**Gelöscht:** the HORUS inlet

**Gelöscht:** figure

**Formatiert:** Schriftart: (Standard) Times New Roman, 10 Pt.

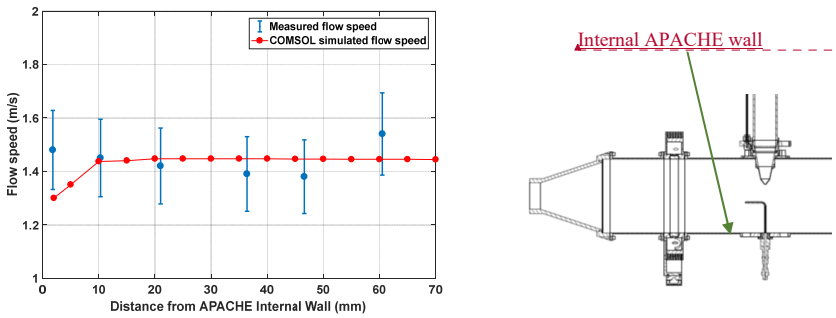


**Figure 6.** The measured (blue) and COMSOL simulated (red) flow speed profiles within APACHE, at 920 hPa. The x-axis is the distance from the internal wall of APACHE. The error bars are quoted to 2σ.

Overall, the modelled flow speed profile did not differ significantly from measured. The only point where the model significantly disagreed with measurements was at the boundary (< 4 mm away from the APACHE wall), where the model predicted a flow speed of 1.3 m $s^{-1}$, which is 6 % lower than the minimum extent of the measurement uncertainty 1.38 m $s^{-1}$. This

disagreement could also be due to the uncertainty in the parametrization of the boundary conditions in the COMSOL simulations. However, as this is occurring within a region that ultimately does not influence the air entering HORUS, see section 4.1.2, the disagreement between modelled and measured flow speeds at distances less than 4 mm from the APACHE wall is ignored. Figure 7 shows the simulated flow speeds at six discrete pressures within APACHE.

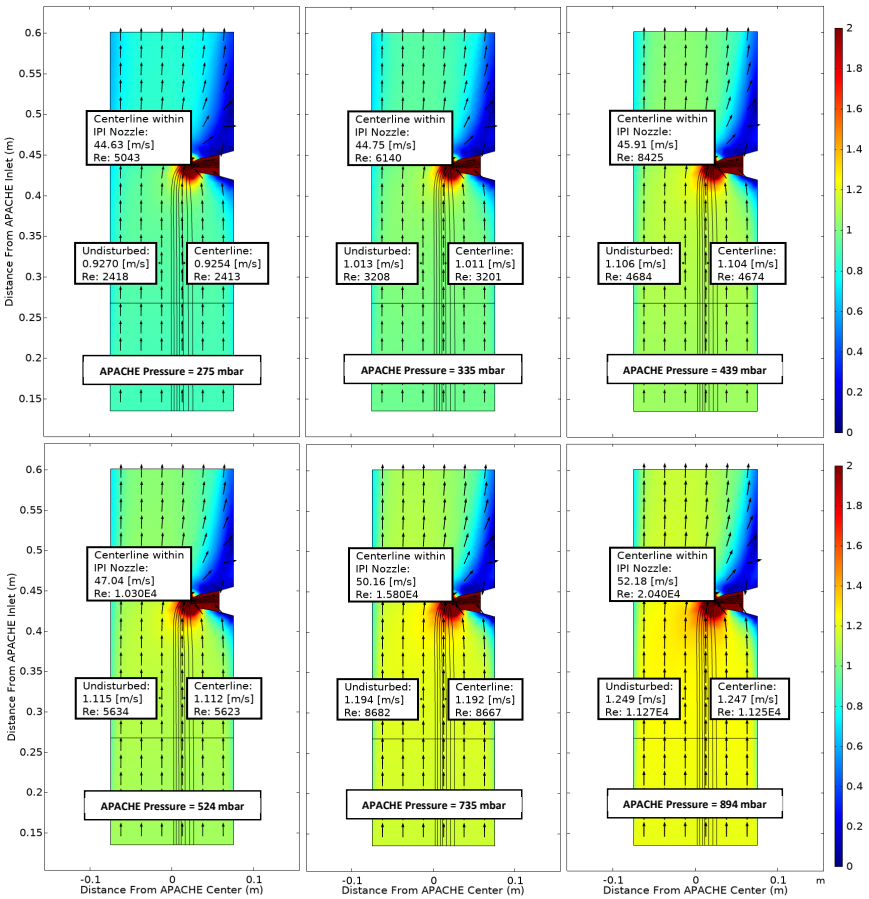


**Figure 7.** COMSOL Multiphysics output data, simulating the flow speed conditions at 6 discrete pressures within APACHE ranging from 275 to 894 mbar, between the sintered filter and the first perforated stainless steel plate. The color represents flow speed in m $s^{-1}$. The black lines are the streamlines created by the HORUS sample flow. The black arrows depict the flow direction. The x-axis is the distance from the center of APACHE in meters. The y-axis is the distance from the APACHE inlet. The "centerline within the IPI nozzle" tags show the flow conditions in the center of the fully formed flows after the HORUS pinhole, the "undisturbed" tags show the flow conditions outside of the HORUS streamlines, and the "centerline" tags show the flow conditions in the center of the streamlines (i.e. the area of flow influenced by HORUS sampling).

**Gelöscht:** Overall, the modelled flow speed ***<Objekt>***profile did not differ significantly from measured. The only point where the model significantly disagreed with measurements was at the boundary (< 4 mm away from the APACHE wall), where the model predicted a flow speed of 1.3 m $s^{-1}$, which is 6 % lower than the minimum extent of the measurement uncertainty 1.38 m $s^{-1}$.

**Gelöscht:**

**Gelöscht:** ¶
¶
¶
¶
¶

**Formatiert:** Schriftart: 14 Pt.

**Formatiert:** Schriftart: (Standard) Times New Roman, 12 Pt.

**Gelöscht:** discreet

**Gelöscht:** discreet

**Gelöscht:** HORUS inlet

**Gelöscht:**

**Formatiert:** Einzug: Erste Zeile: 0 cm

The black lines depict the streamlines of the HORUS sample flow and the color gradient relates to the flow speed. The flow conditions in the center flow within the JPI nozzle, the center of the streamlines and the undisturbed flow airflow not influenced by the sample flow of the HORUS instrument are indicated. The Figure shows the internal APACHE dimensions starting from the sintered filter to the first perforated stainless steel plate 0.135 m and 0.601 m from the APACHE inlet, respectively. From the simulations, the centerline flow speed differs by less than 0.1 % compared to the undisturbed flow, which is also the case at 275 mbar when HORUS is drawing in the highest percentage of the total volume flow entering APACHE. After the sintered filter the high calculated Reynolds numbers (Re > 2300) support the statement that a turbulent flow regime is created. Additionally, the measurements in conjunction with simulations show that the small pores of the sintered filter release a uniform distribution of small turbulent elements across the diameter of APACHE, which remain prevalent all the way up to the JPI nozzle.

### 4.1.2 $HO_X$ losses in APACHE

The modelled OH mixing ratios (pptv) in Figure 8 show the change in OH content as the air flows along the length of APACHE. Mixing ratios were used as they are independent of the changing density within APACHE. In every simulation, the OH and $HO_2$ concentrations were initialized at zero, and losses at the walls were fixed to 100 % for both OH and $HO_2$. The radial photolytic production of OH and $HO_2$, as calculated using Eq. (7) and Eq. (9), occurred when the air passed the UV ring lamp. For all simulations, the $HO_X$ radical-radical recombination loss reactions, (reactions R6-R8), and the measured molecular diffusion coefficient of $OH_{Dm}$ in air (Tang et al., 2014) was used:

$OH_{Dm}$ = 179 (± 20) Torr cm$^2$ s$^{-1}$ (239 ± 27 hPa cm$^2$ s$^{-1}$)

In literature, there have been no reports of successfully performed tests that accurately measure $HO_2$ diffusivity coefficients in air. However, calculations of $HO_2$ diffusion coefficients using the Lennard-Jones potential model have been performed (Ivanov et al., 2007). Ivanov et al. (2007) performed a series of measurements and Lennard-Jones potential model calculations to quantify the polar analogue diffusion coefficients for OH, $HO_2$ and $O_3$ in both air and pure helium. The calculated OH and $O_3$ diffusion coefficients in air from the Lennard-Jones potential model were in good agreement with the recommended measurement values in Tang et al., (2014) well within the given uncertainties. Therefore, to best replicate the diffusivity of $HO_2$ within the simulations, the following diffusion coefficient of $HO_2$ in air from the Ivanov et al., (2007) paper was used:

$HO_{2\,Dm}$ = 107.1 Torr cm$^2$ s$^{-1}$ (142.8 hPa cm$^2$ s$^{-1}$)

It is clear from Figure 8, that irrespective of pressure the air masses at the boundary (where wall losses are 100 %) do not have sufficient time to expand into the HORUS sample flow streamlines, and influence $HO_X$ content entering HORUS. Lateral exchanges between air at the walls of APACHE and the free air in the center are suppressed due to the preservation of the small turbulence regime between the sintered filter and IPI. Table 2 provides, for six pressures, the evolution of OH along the length of APACHE, within the streamlines created by the HORUS sample flow as depicted in Figure 8.

In Table 2, the L term represents OH mixing ratios on the left-most HORUS sample flow streamline shown in Figures 7 and 8. C represents OH mixing ratios in the center of the

**Formatiert:** Schriftart: (Standard) Times New Roman, 12 Pt.
**Gelöscht:** HORUS inlet
**Gelöscht:** post pinhole,
**Gelöscht:** figure
**Gelöscht:**
**Formatiert:** Schriftart: (Standard) Times New Roman, 12 Pt.
**Formatiert:** Schriftart: (Standard) Times New Roman, 12 Pt.
**Gelöscht:** HORUS inlet
**Gelöscht:** ¶
**Formatiert:** Schriftart: (Standard) Times New Roman, 14 Pt.
**Gelöscht:** ¶
**Gelöscht:** ¶
**Gelöscht:** figure
**Gelöscht:** 8
**Gelöscht:** passeed
**Gelöscht:** 8.65
**Gelöscht:** 26.7
**[3] verschoben (Einfügung)**
**Formatiert:** Einzug: Erste Zeile: 0,5 cm
**Gelöscht:** ¶
In literature, there have been no reports of successfully performed tests that accurately measure $HO_2$ diffusivity coefficients in air. However, calculations of $HO_2$ diffusion coefficients using the Lennard-Jones potential model have been performed (Ivanov et al., 2007). Ivanov et al. (2007) performed a series of measurements and Lennard-Jones potential model calculations to quantify the polar analogue diffusion coefficients for OH, $HO_2$ and $O_3$ in both air and pure helium. The calculated OH and $O_3$ diffusion coefficients in air from the Lennard-Jones potential model were in good agreement with the recommended measurement values in Tang et al., (2014) well within the given uncertainties.
**[3] nach oben verschoben:** In literature, there have been no reports of successfully performed tests that accurately measure $HO_2$ diffusivity coefficients in air. However, calculations of $HO_2$ diffusion coefficients using the Lennard-Jones potential model have been performed (Ivanov et al., 2007). Ivanov et al. (2007) performed a series of measurements and Lennard-Jones potential model calculations to quantify the polar analogue diffusion coefficients for OH, $HO_2$ and $O_3$ in both air and pure helium. The calculated OH and $O_3$ diffusion coefficients in air from the Lennard-Jones

HORUS sample flow streamlines shown in Figures 7 and 8. R represents OH mixing ratios on the right-most HORUS sample flow streamline shown in Figures 7 and 8. The mean mixing ratio at each APACHE pressure does not change significantly and is thus independent of the distance from the lamp. Conversely, the standard deviations of the OH mixing ratios within the HORUS sampling streamlines decrease as the distance from the lamp increases, indicating that the air is homogenizing. However, Figure 8 and Table 2, with support from available measurements, indicate that the OH-depleted air masses (i.e. air masses that have experienced loss of OH on the APACHE walls) do not expand into and influence the OH content of air that is being sampled by HORUS. The main loss process that influences $HO_X$ entering HORUS is the wall loss occurring at the IPI nozzle itself. According to the COMSOL simulations, around 22.2 (± 0.8) % (1σ) of OH and $HO_2$ is lost at the nozzle. This value does not significantly change with pressure, indicating that the $HO_X$ loss at the nozzle is pressure independent. As described in section 2.3, the pressure independent sensitivity coefficients are a lump sum value containing the pressure independent wall losses for OH and $HO_2$. Therefore, the characterized pressure independent sensitivity coefficients, shown in section 4.3, have the OH and $HO_2$ losses at the IPI nozzle constrained within them.

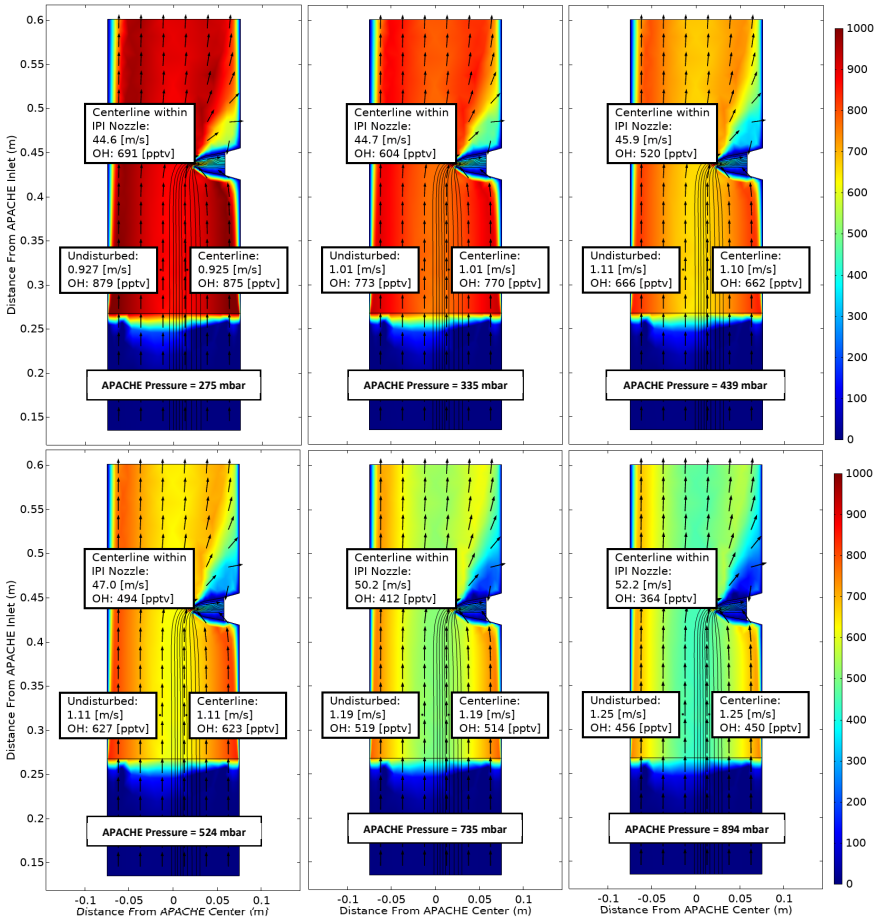


**Figure 8.** COMSOL Multiphysics output data, simulating OH conditions at 6 discrete pressures within APACHE ranging from 275 to 894 mbar, between the sintered filter and the first perforated stainless steel plate. The color is OH mixing ratio (pptv), with initial OH production occurring at the lamp (0.26 m from APACHE inlet), using Eq. (7) and Eq. (9), with water vapour mixing ratios kept constant at 3.2 mmol $mol^{-1}$. The black lines are the streamlines created by the HORUS sample flow. The black arrows depict the flow direction. The x-axis is the distance from the center of APACHE in meters. The y-axis is the distance from the APACHE inlet. The "centerline within IPI nozzle" tags represent the flow and OH concentrations in the center of the fully formed flows after the HORUS pinhole. The "undisturbed" tags show the flow conditions outside of the HORUS streamlines, and the "centerline" tags show the flow conditions in the center of the streamlines (i.e. influenced by HORUS sampling).

**Gelöscht:** discreet

**Gelöscht:** 8

**Gelöscht:** HORUS Inlet t

**Gelöscht:** the area of flow

**Formatiert:** Schriftart: (Standard) +Textkörper (Calibri), 11 Pt., Englisch (Vereinigtes Königreich)

**Table 2.** The evolution of OH within the HORUS sample flow streamlines, along the length of APACHE at all six pressures, within the streamlines created by HORUS sampling as depicted in figure 8. The L term represents OH mixing ratios on the left most streamline, C represents OH mixing ratios in the center of the streamlines, and R represents OH mixing ratios on the right most streamline. The centerline within IPI nozzle column shows the OH mixing ratios in the center of the flow in the HORUS inlet. All standard deviations are quoted to 1σ.

| APACHE Pressure (mbar) | OH (pptv) At the lamp | | | | | OH (pptv) 4.2 cm from lamp | | | | | OH (pptv) 8.4 cm from lamp | | | | | OH (pptv) 12.8 cm from lamp | | | | | OH (pptv) 2 cm before HORUS Inlet | | | | | In Centerline within IPI Nozzle (pptv) |
|---|---|---|---|---|---|---|---|---|---|---|---|---|---|---|---|---|---|---|---|---|---|---|---|---|---|---|
| | L | C | R | Mean | Std (1σ) | L | C | R | Mean | Std (1σ) | L | C | R | Mean | Std (1σ) | L | C | R | Mean | Std (1σ) | L | C | R | Mean | Std (1σ) | |
| 894 | 438 | 445 | 513 | 465 | 41.4 | 442 | 446 | 507 | 465 | 36.4 | 438 | 455 | 500 | 464 | 32.0 | 442 | 456 | 501 | 466 | 30.8 | 445 | 457 | 490 | 464 | 23.3 | 364 |
| 735 | 502 | 508 | 572 | 527 | 38.8 | 506 | 509 | 567 | 527 | 34.4 | 502 | 519 | 560 | 527 | 29.8 | 507 | 519 | 562 | 529 | 28.9 | 509 | 521 | 550 | 527 | 21.1 | 412 |
| 524 | 611 | 617 | 672 | 633 | 33.6 | 615 | 619 | 668 | 634 | 29.5 | 613 | 627 | 660 | 633 | 24.1 | 617 | 628 | 664 | 636 | 24.6 | 619 | 629 | 651 | 633 | 16.4 | 493 |
| 439 | 652 | 657 | 706 | 672 | 29.8 | 656 | 659 | 702 | 672 | 25.7 | 654 | 666 | 698 | 673 | 22.7 | 657 | 667 | 699 | 674 | 21.9 | 660 | 669 | 686 | 672 | 13.2 | 520 |
| 335 | 760 | 765 | 805 | 777 | 24.7 | 764 | 766 | 801 | 777 | 20.8 | 762 | 773 | 799 | 778 | 19.0 | 766 | 774 | 803 | 781 | 19.5 | 768 | 776 | 788 | 777 | 10.1 | 603 |
| 275 | 866 | 871 | 907 | 881 | 22.4 | 870 | 872 | 907 | 883 | 20.8 | 869 | 879 | 904 | 884 | 18.0 | 873 | 880 | 905 | 886 | 16.8 | 875 | 882 | 889 | 882 | 7.0 | 689 |

Gelöscht: s

Gelöscht: N

Gelöscht:



656

## 4.2 UV conditions

The photolysis lamp is housed in a mount with the side facing into the chamber having an anodized aluminum band with thirty 8 mm apertures installed between the lamp and a quartz wall. The housing was flushed with pure nitrogen to purge any $O_2$ present before the lamp was turned on. The nitrogen flushing was kept on continuously thereafter. After approximately one hour, the lamp reached stable operation conditions, i.e the relative flux emitted by the lamp as measured by a photometer (seen in Figure 1b at the UVL on the underside of the APACHE chamber) was constant. The flux ($F_\beta$) entering APACHE is not the same as the flux experienced by the molecules sampled by HORUS ($F$). Factors influencing the ratio between $F_\beta$ and $F$ are as follows. (i) Absorption of light by $O_2$, which is particularly important as $O_2$ has a strong absorption band at 184.9 nm and the $O_2$ density changes in APACHE when calibrating at the different pressures. (ii) The variable radial flux, which is dependent on the geometric setup of the ring lamp and on the location within the irradiation cross section where the molecule is passing. These factors were resolved through the combination of two actinometrical crosscheck methods. The advantage of actinometrical methods is that the flux calculated is derived directly from the actual flux that is experienced by the molecules themselves as they pass through the APACHE chamber.

The first actinometrical method (A) used the HORUS instrument as a transfer standard to relate the flux of a pre-calibrated penray lamp used on the ground based calibration device to $F_\beta$ entering APACHE. This entailed first calibrating the HORUS instrument using a pre-characterized ground based calibration device (Martinez et al., 2010). The pre-calibrated penray lamp flux ($\phi_0$) is calculated from the measured NO concentrations that are produced by irradiating a known mixture of $N_2O$ in a carrier gas:

$$\phi_0 = \frac{(k_a[N_2][M] + k_b[N_2] + k_c[N_2O] + k_d[N_2O][NO])}{2k_d[N_2O]^2\sigma_{N2O}f_{N2O}} \quad (8)$$

where $\sigma_{N2O}$ is the absorption cross section of $N_2O$ at 184.9 nm and $f_{N2O}$ is the correction factor that accounts for the flux reduction via absorption by $N_2O$. A TEI NO monitor measures the NO concentration. For more details on how the ground calibration device is characterized using the photolysis of N2O in conjunction with a TEI NO monitor, see Martinez et al. (2010). Since the pre-characterized ground based calibration device is designed to supply only 50 sL min$^{-1}$, and the sensitivity of airborne HORUS instrument is optimized for high altitude flying, the critical orifice diameter in HORUS was changed from the airborne configuration of 1.4 mm to a 0.8 mm on-ground* configuration. Additionally, the IPI system was switched to passive (i.e. the exhaust line from IPI to the IPI blower was capped). This was to adapt HORUS to a mass flow that the ground based calibration device is able to provide and reduces the internal pressure within HORUS (from 18 mbar to 3.5 mbar) to optimize the sensitivity towards OH at ambient ground level pressures (~1000 mbar). The asterisk discerns terms that were quantified when the smaller 0.8 mm critical orifice was used. The calculated instrument on-ground* sensitivity was then used to translate OH and $HO_2$ concentrations produced by the uv-technik Hg ring lamp into a value for $F_\beta$. Take note that for the direct calibrations of the airborne HORUS system using the characterized APACHE system, discussed in section 4.3, the same initial 1.4 mm diameter critical orifice as used during the airborne campaign was installed. The HORUS on-ground* sensitivities at 1010 mbar for OH and $HO_2$ are 13.7 (± 1.9) cts s$^{-1}$ pptv$^{-1}$ mW$^{-1}$ and 17.9 (± 2.5) cts s$^{-1}$ pptv$^{-1}$ mW$^{-1}$ respectively, with the uncertainties quoted to 1σ. This sensitivity was then used to calculate the OH and $HO_2$ concentrations at the instrument

**Gelöscht:** it

**Gelöscht:** Therefore, allowing direct calibration of the flux inside APACHE itself.

**Gelöscht:** to calibrate the HORUS instrument to be used as a transfer standard

**Formatiert:** Einzug: Erste Zeile: 0 cm

**Formatiert:** Schriftart: Kursiv

**Formatiert:** Schriftart: (Standard) Times New Roman, 12 Pt.

**Formatiert:** Schriftart: 12 Pt.

**Gelöscht:** Only for the purpose of this experiment,

**Gelöscht:** the

**Formatiert:** Nicht Hochgestellt/ Tiefgestellt

**Gelöscht:** 5

**Gelöscht:** re-

**Gelöscht:** ¶

**Gelöscht:**

**Gelöscht:** y

**Gelöscht:** 12

**Gelöscht:** 79

**Gelöscht:** 8

**Gelöscht:** 16.59

**Gelöscht:** 3

nozzle with the APACHE system installed and operating at 1010 mbar. To ensure sufficient flow stability during calibration at this high pressure, the Edwards GSX160 scroll pump was disengaged. Additionally, the water mixing ratios were kept constant (~3.1 mmol mol$^{-1}$) and oxygen levels were varied by adding different pure $N_2$ and synthetic air mixtures, via MFCs. The OH and $HO_2$ concentrations at the IPI nozzle were 1.41 (± 0.01) and 1.31 (± 0.01) x $10^{10}$ molecules cm$^{-3}$ respectively when using a water vapor mixing ratio of 3.1 mmol mol$^{-1}$ in synthetic air injected into APACHE. The uncertainties are quoted as measurement variability at 1σ. Using these values, the OH and $HO_2$ concentrations at the lamp were back calculated accounting for radical-radical loss reactions (R6-R8) and $HO_X$ reactions with $O_3$ (R9-R10) using rate constants taken from Burkholder et al. (2015) with temperature (T) in Kelvin.

$$OH + OH \rightarrow H_2O + O(^3P) \qquad k = 1.8\,x10^{-12} \cdot \exp\left[\frac{1}{T}\right] \qquad \text{(R6)}$$

$$HO_2 + HO_2 \rightarrow H_2O_2 + O_2 \qquad k = 3.0\,x10^{-13} \cdot \exp\left[\frac{460}{T}\right] \qquad \text{(R7)}$$

$$OH + HO_2 \rightarrow H_2O + O_2 \qquad k = 4.8\,x10^{-11} \cdot \exp\left[\frac{250}{T}\right] \qquad \text{(R8)}$$

$$HO_2 + O_3 \rightarrow OH + 2\,O_2 \qquad k = 1.0\,x10^{-14} \cdot \exp\left[\frac{-490}{T}\right] \qquad \text{(R9)}$$

$$OH + O_3 \rightarrow HO_2 + O_2 \qquad k = 1.7\,x10^{-12} \cdot \exp\left[\frac{-940}{T}\right] \qquad \text{(R10)}$$

In APACHE when the Edwards GSX160 scroll pump was disengaged, the transit time between the UV radiation zone and the IPI nozzle was 0.18 seconds, resulting in chemical losses of 30 to 33 % for OH and 27 to 30 % $HO_2$, depending on oxygen concentration. Accounting for these chemical losses yields, OH concentrations of 2.0 (± 0.02) x $10^{10}$ molecules cm$^{-3}$ and $HO_2$ concentrations of 1.9 (± 0.02) x $10^{10}$ molecules cm$^{-3}$ at the lamp, at 1010 mbar. The photon flux ($F$) experienced by the air sampled by HORUS, quantified using the OH and $HO_2$ concentrations stated above, ranged from 3.8 x$10^{14}$ photons cm$^{-2}$ s$^{-1}$ to 6.7 x$10^{14}$ photons cm$^{-2}$ s$^{-1}$ depending on oxygen concentrations and considering the chemical losses. As described before, Eq. (7) shows how the production of OH at the lamp is calculated:

$$[OH] = [H_2O] \cdot \sigma_{H_2O} \cdot F_{184.9\,nm} \cdot \phi_{H_2O} \cdot t \qquad (7)$$

$F_{184.9\,nm}$ is the actinic flux encountered by the water molecules as they pass across the photolysis region, which is dependent on the attenuation of the flux ($F_\beta$) entering APACHE due to water vapor and $O_2$ molecules. Whereas the absorption coefficient of water vapor is constant across the linewidth of the 184.9 nm Hg emission line, the effective absorption cross section of molecular oxygen ($\sigma_{O2}$) changes significantly at 184.9 nm within the linewidth of the Hg lamp (Creasey et al., 2000). Therefore, $\sigma_{O2}$ affecting the APACHE calibrations is dependent on $O_2$ concentration, and the ring lamp temperature and current. Since the operating temperature of the uv-technik Hg lamp and the current applied (0.8 A) was kept constant during the actinometrical experiments and during the APACHE calibrations, any effect on $\sigma_{O2}$ regarding the ring lamp linewidth does not need to be investigated further in this study. The relationship of $F_{184.9\,nm}$ to $F_\beta$ can be derived using Beer-Lambert principles:

$$F_{184.9\,nm} = F_\beta \cdot e^{-(\gamma_{H_2O}[H_2O] + \gamma_{O_2}[O_2])} \qquad (9)$$

where $F_\beta$ is the flux intensity entering APACHE from ring lamp, with:

**Gelöscht:** inlet
**Gelöscht:** HORUS inlet
**Gelöscht:** 51
**Gelöscht:** 43
**Gelöscht:** when only pure synthetic air and water vapor were
**Gelöscht:** ,
**Gelöscht:** t
**Gelöscht:** here
**Gelöscht:**
**Gelöscht:** ¶
**Formatiert:** Einzug: Erste Zeile: 0,5 cm
**Gelöscht:** The chemical losses of OH and $HO_2$ were found to be 32 % and 30%, respectively, yielding
**Gelöscht:** .2
**Gelöscht:**
**Gelöscht:** 2.0
**Gelöscht:**
**Gelöscht:** ,
**Gelöscht:** using a water vapor mixing ratio of 3.1 mmol mol$^{-1}$ in pure synthetic air. The uncertainties are quoted as measurement variability at 1σ.
**Gelöscht:** 75
**Gelöscht:** 1
**Formatiert:** Schriftart: Nicht Kursiv, Nicht Hochgestellt/ Tiefgestellt
**Gelöscht:** absolute
**Gelöscht:** that is
**Gelöscht:** 8
**Gelöscht:** Where

$$\gamma_{O2} = R_\beta \cdot \omega \cdot \sigma_{O2} \quad (10)$$

where $R_\beta$ is the radial distance of the sampled air parcel to the ring lamp of APACHE, ω a correction factor replicating the integrated product of the absorption cross section and the ring lamp's emission line as modified by the effect of the absorption of $O_2$ present in between the lamp and the flight path of the sampled air, normalized by $\sigma_{O2}$ is the effective cross section of $O_2$. When combining Eq. (7) and Eq. (9) the OH concentration produced at the lamp is quantified as:

$$[OH] = [H_2O] \cdot \sigma_{H_2O} \cdot \phi_{H_2O} \cdot t \cdot F_\beta \cdot e^{-(\gamma_{H_2O}[H_2O] + \gamma_{O_2}[O_2])} \quad (11)$$

Eq. (11) can be rearranged to:

$$\ln\left[\frac{[OH]}{[H_2O]}\right] = \ln(F_\beta \cdot t \cdot \phi_{H_2O} \cdot \sigma_{H_2O}) + (-\gamma_{H_2O} \cdot [H_2O] - \gamma_{O_2} \cdot [O_2]) \quad (12)$$

Figure 9, shows the measured production of OH, (left side of Eq. (12)) plotted against oxygen concentration. Given that the other terms within Eq. (12) are constant with changing oxygen levels, the plotted gradient of the linear regression in Figure 9 yields $\gamma_{O2}$ as a function of oxygen concentration being 1.2 x $10^{-19}$ (± 0.05 x$10^{-19}$) $cm^3$ $molecule^{-1}$.

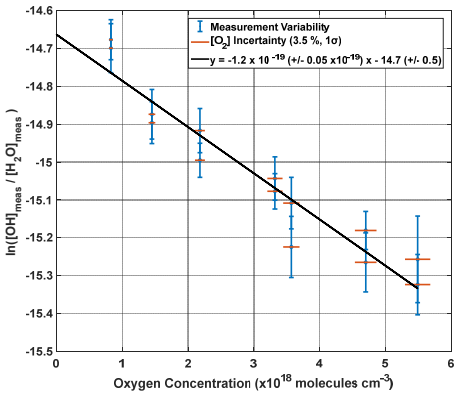


**Figure 9.** Plot showing the result of Eq. (11) as a function of oxygen concentration.

Given that, the y intercept of the linear regression, -14.66, is equal to the natural logarithm of ($F_\beta$ t $\phi_{H2O}$) minus ($\gamma_{H2O}$ [$H_2O$]), the flux entering APACHE $F_\beta$ can be characterized:

$$F_\beta = \left(\frac{e^{-14.66}}{t \cdot \phi H2O}\right) - (\gamma_{H_2O} \cdot [H_2O]) = 6.9 \times 10^{14} (\pm 1.1 \times 10^{14}) \text{ photons cm}^{-2} \text{ s}^{-1} \quad (13)$$

The accuracy in $F_\beta$ from method A is 15.9 % (1σ). Table 3 shows the parameters and their uncertainties contributing to the $F_\beta$ characterized in method A.

**Table 3.** Parameters and uncertainties used in method A, using HORUS as a transfer standard. Overall uncertainty is the sum of the quadrature of the individual uncertainties. O($^1$D) yield is taken from Martinez et al., (2010).

| Parameter | Comments | Total Uncertainty (1σ) |
|---|---|---|
| NO Monitor (TEI) | Calibration uncertainty | 5.2 % |
| NO standard (NPL) | Purity and concentration of the gas | 1 % |
| $N_2O$ cross section | JPL recommendation | 2 % |
| $H_2O$ cross section | JPL recommendation | 2 % |

**Gelöscht:**
**Gelöscht:** 9
**Gelöscht:** Where
**Formatiert:** Schriftart: (Standard) Times New Roman
**Gelöscht:** 8
**Gelöscht:** 10
**Gelöscht:** 10
**Formatiert:** Einzug: Erste Zeile: 0 cm
**Gelöscht:** $\frac{[OH]}{([H_2O] \cdot \sigma_{H_2O})}$
**Gelöscht:** 11
**Gelöscht:** 11
**Gelöscht:** 11
**Gelöscht:** regards to
**Gelöscht:** figure
**Formatiert:** Englisch (Vereinigte Staaten)
**Gelöscht:** 3
**Gelöscht:** ¶
**Gelöscht:** 29.61
**Gelöscht:** $\frac{e^{29.61}}{t \cdot \phi H2O}$
**Gelöscht:** . . . .
**Gelöscht:** . .
**Gelöscht:** 12
**Gelöscht:** this method, which we call
**Gelöscht:** ,
**Formatiert:** Nicht Hochgestellt/ Tiefgestellt
**Gelöscht:** .
**Gelöscht:** involved
**Gelöscht:** The total
**Gelöscht:** (%)
**Formatiert:** Schriftart: 11 Pt.
**Formatierte Tabelle**
**Formatiert:** Schriftart: 11 Pt.
**Formatiert:** Schriftart: 11 Pt.
**Formatiert:** Schriftart: 11 Pt.
**Formatiert:** Schriftart: 11 Pt.
**Formatiert:** Schriftart: 11 Pt.
**Formatiert:** Schriftart: 11 Pt.
**Formatiert:** Schriftart: 11 Pt.
**Formatiert:** Schriftart: 11 Pt.
**Formatiert:** Schriftart: 11 Pt.
**Formatiert:** Schriftart: 11 Pt.

| | | |
|---|---|---|
| $\gamma_{O2}$ | From method A | 3.5 % |
| $O(^1D)$ yield | Martinez et al. (2010) | 1 % |
| Kinetic rate coefficients | JPL recommendation | 12 % |
| $F_\beta$ Variability | From method A | 3.5 % |
| Photolysis chamber dimensions | Specifications of in-house workshop | 3 % |
| $[H_2O]$ | Calibration with NIST standard Dew point generator | 2 % |
| $[O_2]$ | From method A | 3.4 % |
| Mass flow controllers | Calibration with NIST DryCal | 2 % |
| Pressure and Temperature sensors | Validated against NIST standard | 2 % |
| Overall Experimental Stability | Variability of measured terms | 4 % |
| Overall uncertainty | | 15.9 % |

The second actinometrical method (B) involved using an ANSYCO O3 41 M ozone monitor to measure the ozone mixing ratio profile between the JPI nozzle and the wall surface of APACHE, at ground pressure (1021 mbar). This method utilizes $O_2$ photolysis at 184.9 nm, which produces two $O(^3P)$ atoms capable of reacting with a further two $O_2$ molecules to produce $O_3$.

$$O_2 + h\nu \rightarrow O(^3P) + O(^3P) \quad (R11)$$

$$O_2 + O(^3P) + M \rightarrow O_3 + M \quad (R12)$$

The value of 1.2 x$10^{-19}$ $cm^3$ $molecule^{-1}$ for $\gamma_{O2}$ found in the previous method was used to calculate the actinic flux entering APACHE:

$$F_\beta = \frac{[O_3]}{[O_2] \cdot \gamma_{O_2} \cdot \Phi_{O_2} \cdot t \cdot e^{-(\gamma_{O2}[O_2])}} \quad (14)$$

$\Phi_{O2}$ is the quantum yield of $O_2$ at 184.9 nm, which has been determined to be 1 between 242 and 175 nm (Atkinson et al., 2004). As in method A, the ozone produced at the lamp is quantified by back calculating from the ozone measured at the ANSYCO O3 41 M inlet position. Inside APACHE, typical ozone concentrations ranged from 1.26 x$10^{12}$ to 2.05 x$10^{12}$ molecules $cm^{-3}$ depending on the oxygen concentration. From this approach, the calculated $F_\beta$ is 6.11 x $10^{14}$ (± 0.8 x $10^{14}$) photons $cm^{-2}$ $s^{-1}$ with a total uncertainty of 12.9 % (1σ). The final value taken for $F_\beta$ is the average of the two experiments, weighted by their uncertainties:

Actinic flux ($F_\beta$) = 6.37 x $10^{14}$ (± 1.3 x $10^{14}$) photons $cm^{-2}$ $s^{-1}$

Accuracy in $F_\beta$ = 20.5 % (1σ)

Agreement for $F_\beta$ between method A and B, Zeta score = 0.59.

Table 4 shows the parameters and their uncertainties which contribute to the $F_\beta$ characterized in method B.

**Table 4.** Parameters and uncertainties involved in Method B, using ANSYCO O3 41 M monitor. The total uncertainty is the sum of the quadrature of the individual uncertainties.

| Parameter | Comments | Total Uncertainty (1σ) |
|---|---|---|
| $O_3$ calibrator | Calibrated against a primary standard | 2 % |
| $[O_3]$ | Calibration of ANSYCO O3 41 M monitor | 4 % |

Formatiert ... [37]
Formatiert ... [38]
Formatiert ... [39]
Formatiert ... [40]
Formatiert ... [41]
Formatiert ... [42]
Formatiert ... [43]
Formatiert ... [44]
Formatiert ... [45]
Formatiert ... [46]
Formatiert ... [47]
Gelöscht: From c
Formatiert ... [48]
Formatiert ... [49]
Formatiert ... [50]
Formatiert ... [51]
Formatiert ... [52]
Formatiert ... [53]
Formatiert ... [54]
Formatiert ... [55]
Formatiert ... [56]
Formatiert ... [57]
Formatiert ... [58]
Formatiert ... [59]
Gelöscht: ¶
Formatiert ... [60]
Gelöscht: HORUS inlet
Gelöscht: …(R9 ... [61]
Gelöscht: R10
Gelöscht: 3
Gelöscht: 13
Gelöscht: Typical ozone mixing ratios ranged from 4 ... [62]
Gelöscht: 3 …7 x $10^{14}$ (± 0.9….3 x $10^{14}$) photons cm ... [63]
Gelöscht: 14.4
Formatiert ... [64]
Gelöscht: ¶
Formatiert ... [65]
Formatiert ... [66]
Gelöscht: 1σ …1σ% ... [67]
Formatiert ... [68]
Formatiert ... [69]
Formatiert ... [70]
Formatiert ... [71]
Formatiert ... [72]
Formatiert ... [73]
Formatiert ... [74]

| | | |
|---|---|---|
| $[O_2]$ | From method A | 3.4 % |
| $\gamma_{O2}$ | From method A | 3.5 % |
| $F_\beta$ Variability | From method A | 3.5 % |
| Mass flow controllers | Calibration with NIST DryCal | 2 % |
| Pressure and Temperature sensors | Validated against NIST standard | 2 % |
| Experimental Stability | Variability of values | 10.1 % |
| Overall uncertainty | | 12.9 % |

## 4.3 Evaluation of instrumental sensitivity

Figure 10 shows the sensitivity curve of HORUS, the quenching effect, the linear fits used to quantify the pressure independent sensitivity coefficients, and relative $HO_X$ transmission values for OH , OH in the second axis, and $HO_2$ plotted as a function of the HORUS internal density. The red smoothed line in Figure 10 row A represents the calculated sensitivity curve for each measurement using Eq. (4) and the characterized variables therein. Given that this calculated sensitivity curve for each measurement agrees to within 2 sigma of the uncertainties in measured calibration curves, we are confident that each of the terms described in Eq. (4) have been sufficiently resolved. Table 5 shows the ranges, precision and uncertainties of measured or calculated variables affecting OH and $HO_2$ concentrations formed in APACHE.

**Table 5.** Parameters within APACHE, their ranges and uncertainties, contributing to the uncertainty in the three measurement sensitivities within HORUS.

| Parameter (unit) | Range or typical value | Precision (1σ) | Total Uncertainty (1σ) |
|---|---|---|---|
| $F_\beta$ at 184.9 nm (photons $cm^{-2}$ $s^{-1}$) | 6.37 x $10^{14}$ | 3.5 % | 20.5 % |
| $\sigma H_2O$ ($cm^2$ $molecule^{-1}$) | 7.22 x $10^{-20}$ | - | 2 % |
| $\gamma_{O2}$ ($cm^3$ $molecule^{-1}$) | 1.22 x $10^{-19}$ | 1.8 % | 3.5 % |
| $[O_2]$ (x$10^{18}$ molecules $cm^{-3}$) | 1.1 - 4.8 | 1.4 % | 3.4 % |
| $[H_2O]$ (x$10^{16}$ molecules $cm^{-3}$) | 2.00 - 7.41 | 1.2 % | 2 % |
| Mass flow controller (sL $min^{-1}$) | 203 - 988 | < 2 % | 2 % |
| Pressure sensors (mbar) | 275 - 900 | < 1 % | 2 % |
| Temperature sensors (K) | 282 - 302 | < 1 % | 2 % |
| Overall | | 5 % | 21.5 % |

The pressure independent sensitivity coefficients (cN) for OH in the 1st axis (c0), OH in the 2nd axis (c1), and $HO_2$ in the 2nd axis (c2), are calculated by rearranging Eq. (4) to:

$$c0 \cdot \rho_{Int}(P,T) = \frac{C_{OH}(P,T)}{Q_{IF}(P,T) \cdot b_c(T) \cdot [\alpha_{IPI\,OH}(P,T) \cdot \alpha_{HORUS\,OH}(P,T)]} \quad (15)$$

$$c1 \cdot \rho_{Int}(P,T) = \frac{C_{OH(2)}(P,T)}{Q_{IF(2)}(P,T) \cdot b_c(T) \cdot [\alpha_{IPI\,OH}(P,T) \cdot \alpha_{HORUS\,OH(2)}(P,T)]} \quad (16)$$

$$c2 \cdot \rho_{Int}(P,T) = \frac{C_{HO2}(P,T)}{Q_{IF(2)}(P,T) \cdot b_c(T) \cdot [\alpha_{IPI\,HO2}(P,T) \cdot \alpha_{HORUS\,HO2}(P,T)]} \quad (17)$$

The products of Eq. (15 to 17) are plotted against internal density in Figure 10 row C, where the slopes of the linear regressions are the pressure independent sensitivity coefficients. Note that in Eq. (16) and Eq. (17), the bracketed 2 terms are in relation to the OH measurement at the second axis. Table 6 shows the values, precision and uncertainty in the quantified pressure independent sensitivity coefficients.

**Formatiert:** Schriftart: 11 Pt.
**Formatiert:** Schriftart: 11 Pt.
**Formatiert:** Schriftart: 11 Pt.
**Formatiert:** Schriftart: 11 Pt.
**Formatiert:** Schriftart: 11 Pt.
**Formatiert:** Schriftart: 11 Pt.
**Formatiert:** Schriftart: 11 Pt.
**Formatiert:** Schriftart: 11 Pt.
**Formatiert:** Schriftart: 11 Pt.
**Formatiert:** Schriftart: 11 Pt.
**Formatiert:** Schriftart: 11 Pt.
**Formatiert:** Schriftart: 11 Pt.
**Formatiert:** Schriftart: 11 Pt.
**Formatiert:** Schriftart: 11 Pt.
**Gelöscht:** ¶ 5 Results and discussion¶ 5.1
**Gelöscht:**
**Formatiert:** Einzug: Erste Zeile: 0 cm
**Formatiert:** Block
**Formatierte Tabelle**
**Formatiert:** Block
**Formatiert:** Block
**Formatiert:** Block
**Formatiert:** Block
**Formatiert:** Block
**Formatiert:** Block
**Formatiert:** Block
**Formatiert:** Block
**Formatiert:** Block
**Formatiert:** Einzug: Erste Zeile: 0,5 cm
**Gelöscht:** Table 6 shows t
**Gelöscht:** found from the slopes in figure 10 row C.
**Formatiert:** Einzug: Erste Zeile: 0,5 cm

**Table 6.** Pressure independent sensitivities and their overall uncertainty from calibrations with APACHE.

| Parameter (cts $pptv^{-1}$ $s^{-2}$ $cm^3$ $molecule^{-1}$ $mW^{-1}$) | Value ($x10^{-9}$) | Precision (± 1σ) | Total Uncertainty (1σ) |
|---|---|---|---|
| c0 for OH in OH axis | 3.8 | 4 % | 6.9 % |
| c1 for OH in $HO_2$ axis | 2.3 | 4 % | 6.9 % |
| c2 for $HO_2$ in $HO_2$ axis | 4.5 | 2 % | 5.6 % |

**Gelöscht:**

**Formatiert:** Block

**Formatiert:** Schriftart: 11 Pt.

**Formatiert:** Schriftart: 11 Pt.

**Formatiert:** Block

**Formatiert:** Schriftart: 11 Pt.

**Formatiert:** Schriftart: 11 Pt.

**Formatiert:** Block

**Formatiert:** Schriftart: 11 Pt.

**Formatiert:** Schriftart: 11 Pt.

**Formatiert:** Schriftart: 11 Pt.

**Formatiert:** Block

**Formatiert:** Schriftart: 11 Pt.

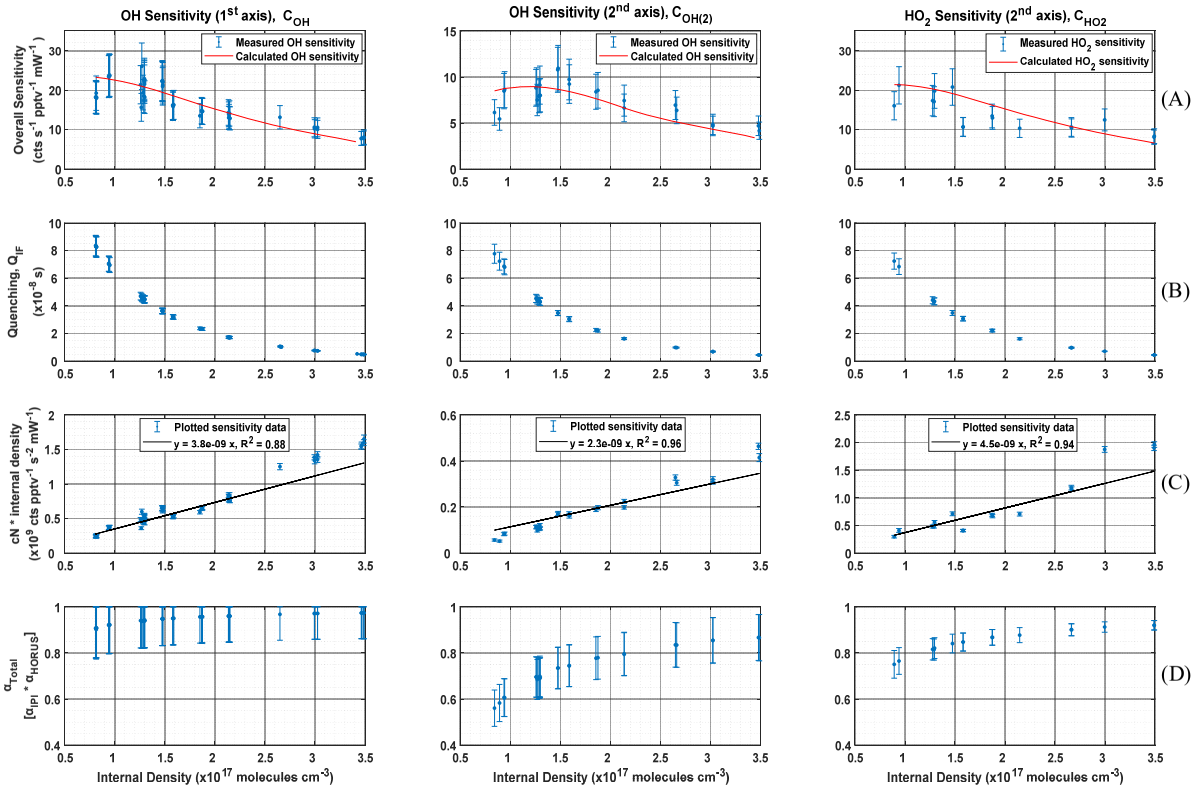


**Figure 10.** The determination of the pressure based sensitivity of OH in both axes and $HO_2$ for HORUS. The data shown are one-hour averages for the tested pressures, all plotted with the internal density on the x-axis. The top row (A) is the measured (blue data points) HORUS sensitivity curve and calculated (red line) sensitivity curve. The second row (B) is internal quenching by $N_2$, $O_2$, and water vapor, and row (C) is internal density and cN (c0 for OH 1st axis, c1 for OH 2nd axis and c2 for $HO_2$), (D) is the total OH and $HO_2$ transmissions, all plotted against internal density. The error bars represent measurement variability (1σ), for rows B and C. In rows A and D, the error bars represent the total uncertainty (1σ).

**Formatiert:** Einzug: Erste Zeile: 0 cm

**Formatiert:** Englisch (Vereinigte Staaten)

**Gelöscht:** ,

**Gelöscht:** t

In Figure 10, row C the quenching ($Q_{IF}$) is plotted against internal density. $Q_{IF}$ is calculated using the same approach as described in Faloona et al. (2004) and Martinez et al. (2010):

$$Q_{IF}(P) = \frac{1}{\Gamma}\left(e^{-\Gamma g_1} - e^{-\Gamma g_2}\right) \quad (18)$$

where Γ is the excited state decay frequency (Hz), consisting of the natural decay frequency, and decay due to collisional quenching that is dependent on pressure, temperature, and water vapor mixing ratio. $g_1$ and $g_2$ are the detector gate opening and closing times after the initial excitation laser pulse, which are set to 104 ns and 600 ns respectively.

As described in section 2.3, the pressure independent sensitivity coefficients are lump sum variables containing pressure independent $HO_X$ wall loss. The pressure dependent $HO_X$ transmission through the HORUS instrument is quantified and described below. In-flight, IPI operates across the pressure range of 180 to 1010 mbar. However, within HORUS, post critical orifice, at detection axes where $HO_X$ is measured the pressure ranges from 3.1 to 18.4 mbar. Therefore, the transmission through IPI ($\alpha_{IPI}$) and through HORUS ($\alpha_{HORUS}$) must be quantified separately using the corresponding measured pressures and transit times, before being combined as the total transmission ($\alpha_{IPI} \cdot \alpha_{HORUS} = \alpha_{Total}$). To calculate the transmission of $HO_X$ within IPI, the following was used:

$$\alpha_{IPI\,OH} = 1 - \left[\frac{OH_{DM}(P) \cdot t_{r\,IPI}(P,T) \cdot \pi}{IPI_A \cdot P_{IPI}}\right] \quad (19)$$

$$\alpha_{IPI\,HO_2} = 1 - \left[\frac{HO_{2\,DM}(P) \cdot t_{r\,IPI}(P,T) \cdot \pi}{IPI_A \cdot P_{IPI}}\right] \quad (20)$$

where $t_{rIPI}$ is the transit time within IPI, i.e. the time it takes for air to flow from the IPI nozzle to the critical orifice of HORUS. $IPI_A$ is the internal cross sectional area of IPI and $P_{IPI}$ is the measured pressure within IPI. The $OH_{DM}$ and $HO_{2\,DM}$ terms are the OH and $HO_2$ diffusion coefficients as described in section 4.1.2. $\alpha_{IPI\,OH}$ is the transmission of OH through IPI, and $\alpha_{IPI\,HO2}$ is the transmission of $HO_2$ through IPI. By applying Eq. (19) and Eq. (20), $\alpha_{IPI\,OH}$ and $\alpha_{IPI\,HO2}$ ranged from 0.97 to 0.99 and 0.99 to 0.997 respectively across the pressure range within IPI of 198 – 808 mbar and IPI transit times of 90 – 120 milliseconds. However, to calculate $\alpha_{Total}$, the OH and $HO_2$ transmission post critical orifice, $\alpha_{HORUS\,OH}$ and $\alpha_{HORUS\,HO2}$, must be resolved. $\alpha_{HORUS}$ regarding OH and $HO_2$ can be calculated by adapting Eq. (19) and Eq. (20) to the internal HORUS conditions producing:

$$\alpha_{HORUS\,OH} = 1 - \left[\frac{OH_{DM}(P) \cdot t_{r1}(P,T) \cdot \pi}{HORUS_A \cdot P_{int}}\right] \quad (21)$$

$$\alpha_{HORUS\,OH(2)} = 1 - \left[\frac{OH_{DM}(P) \cdot t_{r2}(P,T) \cdot \pi}{HORUS_A \cdot P_{int}}\right] \quad (22)$$

$$\alpha_{HORUS\,HO_2} = 1 - \left[\frac{HO_{2\,DM}(P) \cdot t_{r2}(P,T) \cdot \pi}{HORUS_A \cdot P_{int}}\right] \quad (23)$$

where $t_{r1}$ and $t_{r2}$ are the transit times within HORUS from the critical orifice to the 1st and 2nd detection axis respectively. $HORUS_A$ is the internal cross sectional area of HORUS and $P_{int}$ is the measured internal pressure within HORUS. The OH transmission from the critical orifice to the 1st detection cell ($\alpha_{HORUS\,OH}$) ranged from 0.93 to 0.98, the OH transmission from the critical orifice to the 2nd detection cell ($\alpha_{HORUS\,OH\_2}$) ranged from 0.58 to 0.87, and the $HO_2$ transmission from the critical orifice to the 2nd detection cell ($\alpha_{HORUS\,HO2}$) ranged from 0.76 to 0.92. These ranges are quoted under the HORUS internal pressure range of 3.7 to 13.7 mbar

**Formatiert:** Block
**Formatiert:** Einzug: Erste Zeile: 0,5 cm
**Gelöscht:** 3.2
**Formatiert:** Nicht Hochgestellt/ Tiefgestellt
**Gelöscht:** the pressure driven wall losses in IPI and post critical orifice both contribute to the overall sensitivity curve. The OH transmission terms ($\alpha_{IPI}$ and $\alpha_{HORUS}$) can be considered together
**Gelöscht:** OH
**Gelöscht:** According to the COMSOL simulations, the losses of $HO_X$ occur mainly at the inlet itself resulting in for both OH and $HO_2$ to be 78 (± 0.8, full range) %.
**Gelöscht:** loss
**Gelöscht:** 4
**Gelöscht:** 15
**Gelöscht:** W
**Gelöscht:** inlet
**Gelöscht:** 14
**Gelöscht:** 15
**Gelöscht:** 8
**Gelöscht:** 5
**Gelöscht:** 210
**Gelöscht:** 1010
**Gelöscht:** Summing the inlet wall loss found from the COMSOL simulations (78 ± 0.8 %) and $\alpha_{IPI\,OH}$ and $\alpha_{IPI\,HO2}$ calculated from Eq. (14) and Eq. (15) results in a combined $\alpha_{IPI}$ term for OH of 76.7 (± 2.2, full range) and for $HO_2$ of 77.3 (± 1.6, full range).
**Gelöscht:** 14
**Gelöscht:** 15
**Formatiert:** Schriftart: Englisch (Vereinigte Staaten)
**Gelöscht:** 16
**Gelöscht:** _
**Gelöscht:** 2
**Gelöscht:** 17

and internal transit times to the 1st detection axis (3.8 to 4.3 milliseconds) and 2nd detection axis (23.5 to 27.8 milliseconds). The combined $\alpha_{Total}$ values for OH, OH at the second detection axis, and $HO_2$ are plotted in Figure 10 row D as a function of the internal density of HORUS. Table 7 shows the calculated $\alpha_{Total}$ transmission terms, their precision and uncertainty for OH to the first axis, OH to the second axis, and $HO_2$ to the second axis.

**Table 7.** Pressure dependent OH and $HO_2$ transmission and their overall uncertainty from calibrations with APACHE.

| Parameter (%) | Value | Precision (± 1σ) | Total Uncertainty (1σ) |
|---|---|---|---|
| $\alpha_{Total}$ (for OH to OH axis) | 90 - 97 | 2.8 % | 14.3 – 11.5 % |
| $\alpha_{Total}$ (for OH to $HO_2$ axis) | 56 - 86 | 4.3 % | 14.1 – 11.5 % |
| $\alpha_{Total}$ (for $HO_2$ to $HO_2$ axis) | 75 - 92 | 2.9 % | 7.9 – 2.2 % |

Table 8 shows the measured sensitivity values using APACHE for OH at the first axis ($C_{OH}$), OH at the second axis ($C_{OH\,(2)}$), and $HO_2$ at the second axis ($C_{HO2}$). The precision denotes the 1σ variability in the measured $HO_X$ signals from HORUS, the total uncertainty is the root sum square of the total uncertainty values from the variables listed in Tables 5 and 6.

**Table 8.** Pressure dependent sensitivities for the three measurement within HORUS, their overall uncertainty from calibrations with APACHE. The range in the precision relates to the numbers quoted in the value column.

| Parameter (unit) | Value | Precision (± 1σ) | Total Uncertainty (1σ) |
|---|---|---|---|
| $C_{OH}$ (cts $s^{-1}$ $pptv^{-1}$ $mW^{-1}$) | 7.8 - 26.1 | 1.1 - 0.5 % | 22.6 % |
| $C_{OH\,(2)}$ (cts $s^{-1}$ $pptv^{-1}$ $mW^{-1}$) | 4.2 – 11.0 | 2.0 - 0.3 % | 22.6 % |
| $C_{HO2}$ (cts $s^{-1}$ $pptv^{-1}$ $mW^{-1}$) | 8.1 – 21.2 | 0.4 - 0.7 % | 22.2 % |

The undescribed remaining fraction that influences the instrument sensitivity ($R_{undescribed}$), is calculated by dividing the overall sensitivity values by described in Eq. (4):

$$R_{OH} = \frac{C_{OH}}{c0 \cdot \rho_{Int}(P,T) \cdot Q_{IF}(P,T) \cdot b_c(T) \cdot [\alpha_{IPI\,OH}(P,T) \cdot \alpha_{HORUS\,OH}(P,T)]} \quad (24)$$

$$R_{OH\,(2)} = \frac{C_{OH(2)}}{c1 \cdot \rho_{Int}(P,T) \cdot Q_{IF\,(2)}(P,T) \cdot b_c(T) \cdot [\alpha_{IPI\,OH}(P,T) \cdot \alpha_{HORUS\,OH(2)}(P,T)]} \quad (25)$$

$$R_{HO_2} = \frac{C_{HO2}}{c2 \cdot \rho_{Int}(P,T) \cdot Q_{IF\,(2)}(P,T) \cdot b_c(T) \cdot [\alpha_{IPI\,HO2}(P,T) \cdot \alpha_{HORUS\,HO2}(P,T)]} \quad (26)$$

$$R_{undescribed} = \{R_{OH}\,;\ R_{OH\,(2)}\,;\ R_{HO_2}\}$$

where $R_{undescribed}$ is a matrix containing the undescribed remain factors from the three measurements. When plotting $R_{undescribed}$ against the internal pressure of HORUS, (see supplementary, Figure. S10), the data scatters ± 0.15 (1σ) about the average value of 1.02 (± 0.23, 1σ calibration uncertainty). This means that (as an upper limit) <2 % of the overall instrument sensitivity is unresolved by the terms described in Eq. (4). Additionally, the 1σ variability of the $R_{undescribed}$ is 34 % smaller than the uncertainty in the APACHE calibration, meaning that this remaining fraction is declared as neither pressure dependent nor pressure independent.

[1] verschoben (Einfügung)
Formatiert ... [75]
Formatiert ... [76]
Gelöscht: 7
Gelöscht: 2
Formatiert ... [77]
Formatiert ... [78]
Gelöscht: 61
Formatiert ... [80]
Gelöscht: 4
Formatiert ... [79]
Formatiert ... [81]
Formatiert ... [82]
Formatiert ... [83]
Gelöscht: 35
Formatiert ... [84]
Gelöscht: 65
Formatiert ... [85]
Formatiert ... [86]
Formatiert ... [87]
Gelöscht: 54
Formatiert ... [88]
Gelöscht: 70
Formatiert ... [89]
Gelöscht: -
Formatiert ... [90]
Gelöscht: 4.7
Formatiert ... [91]
Formatiert ... [92]
Formatiert ... [93]
Formatiert ... [95]
Formatiert ... [94]
Formatiert ... [96]
Formatiert ... [97]
Formatiert ... [98]
Formatiert ... [99]
Formatiert ... [100]
Formatiert ... [101]
Formatiert ... [102]
Formatiert ... [103]
Formatiert ... [104]
Formatiert ... [105]

It is important to note here that all data shown in Figure 10, with the exception of the pressure independent sensitivity coefficients, are in relation to temperatures and pressures HORUS experienced during calibrations in the lab. To apply these findings to real airborne measurements, the pressure and temperature dependent terms in Eq. (4) are calculated using the temperatures and pressures that are measured within the instrument during flight. The only terms that affect measurement sensitivity and are directly transferable from the calibrations with APACHE to the measurements in-flight shown in Eq. (4) are the pressure independent sensitivity coefficient as they are not subject to change with the large temperature and pressures ranges HORUS experiences when airborne. Figure 11 shows the pressure and temperature dependent terms from Eq. (4) characterized for a typical flight that took place during the OMO-ASIA 2015 airborne campaign. In Figure 11, the sensitivity values, limit of detection, transmission values for OH (blue data points) and $HO_2$ (red data points), and the ambient water mixing ratios (black date points) that occurred during flight 23 are plotted as a function of altitude. During flight, the OH sensitivity ranged from 5.4 (± 1.2) cts $s^{-1}$ $pptv^{-1}$ $mW^{-1}$ on ground to 24.1 (± 5.4) cts $s^{-1}$ $pptv^{-1}$ $mW^{-1}$ at 14 km. The HORUS sensitivity values for $HO_2$ ranged from 5.5 (± 1.2) cts $s^{-1}$ $pptv^{-1}$ $mW^{-1}$ and reached an average maxima of 20.5 (± 4.5) cts $s^{-1}$ $pptv^{-1}$ $mW^{-1}$ at 11.4 km. Above 11.4 km the $HO_2$ sensitivity decreased with altitude reaching 19.7 (± 4.4) cts $s^{-1}$ $pptv^{-1}$ $mW^{-1}$ at 14 km. This drop in $HO_2$ sensitivity is attributable to the increasing decline in $HO_2$ transmission inside HORUS as the aircraft flies higher, despite the sensitivity improvements via quenching as the air is becoming drier. The water vapor mixing ratios at 14 km on average are three orders of magnitude lower than the average water vapor mixing ratio of 1.5 % at ground level; which greatly suppresses quenching of OH and thus is the main driver for the general increasing trend in the instrument sensitivity towards $HO_X$ as altitude increases. Additionally, Figure 11 shows that the limit of detection for both OH and $HO_2$ decrease with increasing altitude. For OH, the HORUS limit of detection is ~0.11 pptv at ground level and drops to ~0.02 pptv at 14 km. For $HO_2$ the limit of detection is ~1.2 pptv at ground level and drops to 0.23 pptv at 14 km.

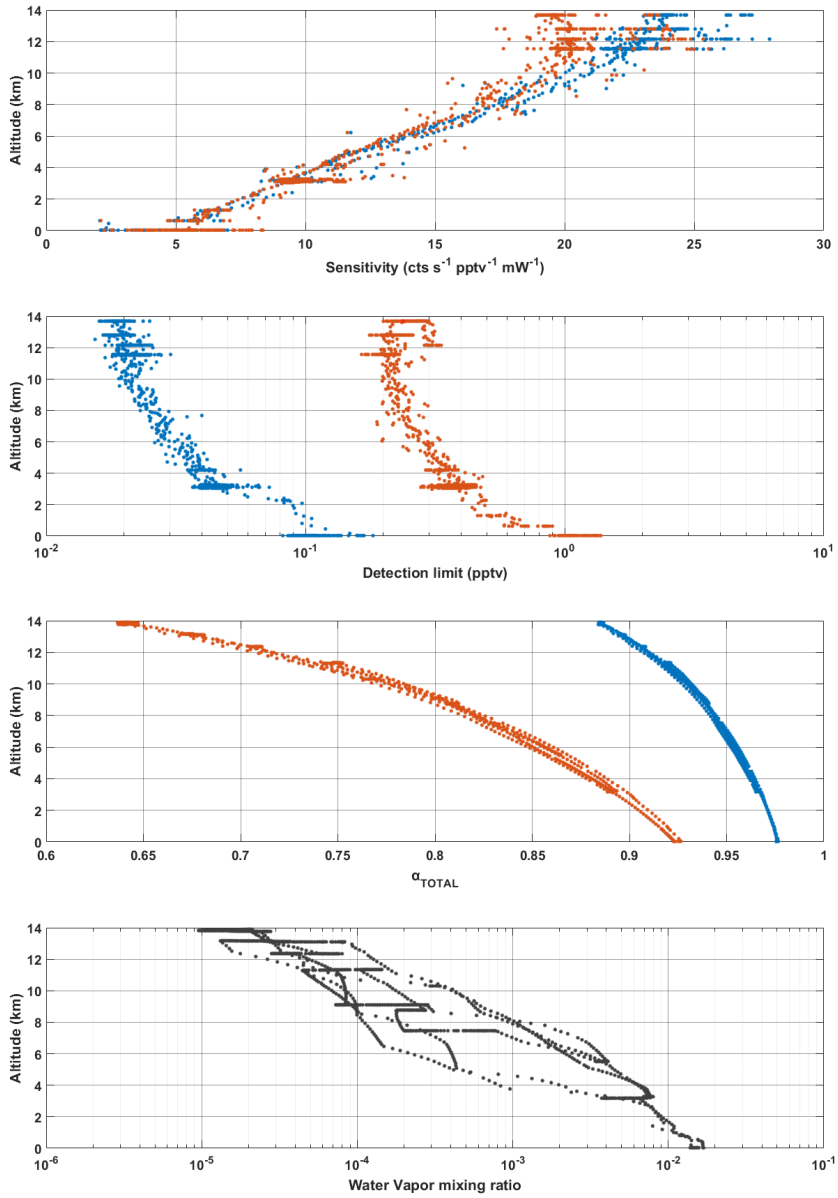


**Figure 11.** In-flight, sensitivity curves, limit of detection, and $HO_X$ transmission plotted against altitude for OH (blue data points) and $HO_2$ (red data points, and the water vapour mixing ratio (black data points) plotted against altitude in km (bottom plot). Data taken from flight 23.

**[1] nach oben verschoben:** ¶

**Gelöscht:** *a series of sDuring flight, the816.455.52an average 17.53.95 , despite* ***<Objekt>***¶
**Table 8.** Pressure dependent sensitivities for the three measurement within HORUS, their overall uncertainty from calibrations with APACHE. The range in the precision relates to the numbers quoted in the value column.¶
Parameter (unit)¶
... [106]

**Gelöscht:** 9

**Gelöscht:** Plot showing the result of Eq. (11) as a function of oxygen concentration.

**Gelöscht:**

## 5 Conclusions

The overall goal of this study was to develop and test a new calibration system capable of providing the high flows required by the airborne HORUS system whilst maintaining stable pressures across the pressure ranges experienced during flight. Such systems are critical to suitably characterize airborne systems, (such as a LIF-FAGE measuring $HO_X$), that have a strong pressure dependent sensitivity. In addition, this system is purely based on the use of water-vapor photolysis, which is a frequently adopted technique for $HO_X$ instrument calibration (Martinez et al., 2003; Faloona et al., 2004; Dusanter et al., 2008). The COMSOL multiphysics simulations constrained by temperature, pressure and mass flow measurements demonstrated that air masses at the boundary of the APACHE system do not have sufficient time to expand into the streamlines created by the HORUS sample flow and influence the $HO_X$ content entering HORUS. The largest uncertainties result from constraining the flux ($F_\beta$) entering APACHE (6.37 ± 1.3 x $10^{14}$ photons $cm^{-2}$ $s^{-1}$, 1σ) and the total uncertainty in the pressure independent sensitivity coefficients (ranging from 5.6 to 6.9 %, 1σ). The two actinometrical methods used to derive $F_\beta$ proved to be in good agreement with a zeta score of 0.59, considering 1σ of their uncertainties. The HORUS transfer standard method yielded an $F_\beta$ value of 6.9 ± 1.1 x $10^{14}$ photons $cm^{-2}$ $s^{-1}$ (1σ) and the ozone monitor method yielded an $F_\beta$ value of 6.11 ± 0.8 x $10^{14}$ photons $cm^{-2}$ $s^{-1}$ (1σ). Furthermore, the APACHE system enabled the total OH and $HO_2$ pressure dependent transmission factors to be characterized as a function of internal pressure. Calculations of $HO_X$ diffusivity to the walls within IPI and the low-pressure regime within HORUS yielded 90 - 97 % for OH transmission to the first detection axis, 56 - 86 % for OH transmission to the second detection axis, and 75 - 92 % for $HO_2$ transmission to the second detection axis. Future studies with APACHE are planned to expand upon the findings within this paper with a particular focus on temperature control and on improving operational pressure and flow speed ranges. However, in this study, the APACHE calibration system has demonstrated that, within the lab, it is sufficiently capable of calibrating the airborne HORUS instrument across the pressure ranges the instrument had experienced in-flight during the OMO-ASIA 2015 airborne campaign. The overall uncertainty of 22.1 – 22.6 % (1σ) demonstrates that this calibration approach with APACHE compares well with other calibration methods described earlier in Table 1. Nevertheless, there is potential for improvement. Accurate calibrations of instruments, particularly airborne instruments that have strong pressure dependent sensitivities, are critical to acquiring concentrations of atmospheric species with minimal uncertainties. Only through calibrations can the accuracy of measurements be characterized and allow for robust comparisons with other measurements and with models to expand our current understanding of chemistry that occurs within our atmosphere.

*Author contributions.* K.H, C.E, M.M, H.H, U.J, and M.R formulated the original concept and designed the APACHE system. D.M, H.H, and U.J prototyped, developed, and characterized the APACHE system. T.K, D.M, and H.H developed and performed the CFD simulations. D.M prepared the manuscript with contributions from all coauthors.

*Acknowledgments.* We would like to take this opportunity to give a thank you to the in-house workshop at the Max Planck Institute for Chemistry for construction and guidance in the development of APACHE. Additionally, a special thank you to Dieter Scharffe for his assistance and advice during the development stage of this project.

**Gelöscht:** ¶ 6

**Formatiert:** Englisch (Vereinigte Staaten)

**Formatiert:** Einzug: Erste Zeile: 0,5 cm

**Gelöscht:** The main $HO_X$ wall losses occurred at the HORUS inlet where on average 23.3 % (± 1.6, full range) of OH and 22.7 % (± 0.9, full range) of $HO_2$ are lost. While the application of these factors contribute to the uncertainty in the overall calibration factor, they proved to be critical in understanding and constraining the UV conditions within APACHE.

**Gelöscht:** 0.9

**Gelöscht:** $s^{-1}$

**Gelöscht:** one another

**Gelöscht:** ,

**Gelöscht:** with t

**Gelöscht:** yielding

**Gelöscht:** yielding

**Gelöscht:** 5.7

**Gelöscht:** 74

**Gelöscht:** $s^{-1}$

**Gelöscht:** using both COMSOL simulations and c

**Gelöscht:** Overall

**Gelöscht:** sufficiently able to calibrate

**Gelöscht:** system

**Gelöscht:** during

**Gelöscht:** relatively low

**Gelöscht:** 17

**Gelöscht:** -

**Gelöscht:** 18

**Gelöscht:** the suitability of

**Gelöscht:** , particularly when compared

**Gelöscht:** to

**Gelöscht:** ¶

## References

Gelöscht: ¶
¶
¶
¶
¶


Albrecht, S. R., A. Novelli, A. Hofzumahaus, S. Kang, Y. Baker, T. Mentel, A. Wahner and H. Fuchs, "Measurements of hydroperoxy radicals (HO2) at atmospheric concentrations using bromide chemical ionisation mass spectrometry." Atmospheric Measurement Techniques **12,**2: 891-902, 2019.

Atkinson, R., D. L. Baulch, R. A. Cox, J. N. Crowley, R. F. Hampson, R. G. Hynes, M. E. Jenkin, M. J. Rossi and J. Troe, "Evaluated kinetic and photochemical data for atmospheric chemistry: Volume I - gas phase reactions of O-x, HOx, NOx and SOx species." Atmospheric Chemistry and Physics **4**: 1461-1738, 2004.

Brauers, T., U. Aschmutat, U. Brandenburger, H. P. Dorn, M. Hausmann, M. Hessling, A. Hofzumahaus, F. Holland, C. PlassDulmer and D. H. Ehhalt, "Intercomparison of tropospheric OH radical measurements by multiple folded long-path laser absorption and laser induced fluorescence." Geophysical Research Letters **23,**18: 2545-2548, 1996.

Brauers, T., M. Hausmann, A. Bister, A. Kraus and H. P. Dorn, "OH radicals in the boundary layer of the Atlantic Ocean 1. Measurements by long-path laser absorption spectroscopy." Journal of Geophysical Research-Atmospheres **106,**D7: 7399-7414, 2001.

Brune, W. H., P. S. Stevens and J. H. Mather, "Measuring OH and HO2 in the Troposphere by Laser-Induced Fluorescence at Low-Pressure." Journal of the Atmospheric Sciences **52,**19: 3328-3336, 1995.

Burkholder, J. B., S. P. Sander, J. Abbatt, J. R. Barker, R. E. Huie, C. E. Kolb, M. J. Kurylo, V. L. Orkin, D. M. Wilmouth and P. H. Wine, "Chemical Kinetics and Photochemical Data for Use in Atmospheric Studies, Evaluation No. 18." JPL Publication 15-10, 2015.

Cantrell, C. A., G. D. Edwards, S. Stephens, L. Mauldin, E. Kosciuch, M. Zondlo and F. Eisele, "Peroxy radical observations using chemical ionization mass spectrometry during TOPSE." Journal of Geophysical Research-Atmospheres **108,**D6, 2003.

COMSOL, Multiphysics Documentation, version 5.4, [software], 2019.

Creasey, D. J., G. E. Evans, D. E. Heard and J. D. Lee, "Measurements of OH and HO2 concentrations in the Southern Ocean marine boundary layer." Journal of Geophysical Research-Atmospheres **108,**D15, 2003.

Creasey, D. J., D. E. Heard and J. D. Lee, "Absorption cross-section measurements of water vapour and oxygen at 185 nm. Implications for the calibration of field instruments to measure OH, HO2 and RO2 radicals." Geophysical Research Letters **27,**11: 1651-1654, 2000.

Dieke, G. H. and H. M. Crosswhite, "The Ultraviolet Bands of OH - Fundamental Data." Journal of Quantitative Spectroscopy & Radiative Transfer **2,**2: 97-&, 1962.

Dilecce, G., P. F. Ambrico and S. De Benedictis, "An ambient air RF low-pressure pulsed discharge as an OH source for LIF calibration." Plasma Sources Science & Technology **13,**2: 237-244, 2004.

Dorn, H. P., R. Neuroth and A. Hofzumahaus, "Investigation of OH Absorption Cross-Sections of Rotational Transitions in the a(2)Sigma(+), V'=0 [- X(2)Pi, V''=0 Band under Atmospheric Conditions - Implications for Tropospheric Long-Path Absorption-Measurements." Journal of Geophysical Research-Atmospheres **100,**D4: 7397-7409, 1995.

Dusanter, S., D. Vimal and P. S. Stevens, "Technical note: Measuring tropospheric OH and HO2 by laser-induced fluorescence at low pressure. A comparison of calibration techniques." Atmospheric Chemistry and Physics **8,**2: 321-340, 2008.

Engel, V., V. Staemmler, R. L. Vanderwal, F. F. Crim, R. J. Sension, B. Hudson, P. Andresen, S. Hennig, K. Weide and R. Schinke, "Photodissociation of Water in the 1st Absorption-Band - a Prototype for Dissociation on a Repulsive Potential-Energy Surface." Journal of Physical Chemistry **96,**8: 3201-3213, 1992.

Faloona, I. C., D. Tan, R. L. Lesher, N. L. Hazen, C. L. Frame, J. B. Simpas, H. Harder, M. Martinez, P. Di Carlo, X. R. Ren and W. H. Brune, "A laser-induced fluorescence instrument for detecting

tropospheric OH and HO2: Characteristics and calibration." Journal of Atmospheric Chemistry **47,**2: 139-167, 2004.

Freeman, A. J., "Configuration Interaction Study of the Electronic Structure of the OH Radical by the Atomic and Molecular Orbital Methods." Journal of Chemical Physics **28,**2: 230-243, 1958.

Fuchs, H., B. Bohn, A. Hofzumahaus, F. Holland, K. D. Lu, S. Nehr, F. Rohrer and A. Wahner, "Detection of HO2 by laser-induced fluorescence: calibration and interferences from RO2 radicals." Atmospheric Measurement Techniques **4,**6: 1209-1225, 2011.

Fuchs, H., Z. F. Tan, A. Hofzumahaus, S. Broch, H. P. Dorn, F. Holland, C. Kunstler, S. Gomm, F. Rohrer, S. Schrade, R. Tillmann and A. Wahner, "Investigation of potential interferences in the detection of atmospheric ROx radicals by laser-induced fluorescence under dark conditions." Atmospheric Measurement Techniques **9,**4: 1431-1447, 2016.

Hard, T. M., L. A. George and R. J. O'brien, "Fage Determination of Tropospheric OH and $HO_2$." Journal of the Atmospheric Sciences **52,**19: 3354-3372, 1995.

Hard, T. M., L. A. George and R. J. O'Brien, "An absolute calibration for gas-phase hydroxyl measurements." Environmental Science & Technology **36,**8: 1783-1790, 2002.

Heard, D. E. and M. J. Pilling, "Measurement of OH and HO2 in the troposphere." Chemical Reviews **103,**12: 5163-5198, 2003.

Hens, K., A. Novelli, M. Martinez, J. Auld, R. Axinte, B. Bohn, H. Fischer, P. Keronen, D. Kubistin, A. C. Nolscher, R. Oswald, P. Paasonen, T. Petaja, E. Regelin, R. Sander, V. Sinha, M. Sipila, D. Taraborrelli, C. T. Ernest, J. Williams, J. Lelieveld and H. Harder, "Observation and modelling of HOx radicals in a boreal forest." Atmospheric Chemistry and Physics **14,**16: 8723-8747, 2014.

Hofzumahaus, A., T. Brauers, U. Aschmutat, U. Brandenburger, H. P. Dorn, M. Hausmann, M. Hessling, F. Holland, C. PlassDulmer, M. Sedlacek, M. Weber and D. H. Ehhalt, "The measurement of tropospheric OH radicals by laser-induced fluorescence spectroscopy during the POPCORN field campaign and Intercomparison of tropospheric OH radical measurements by multiple folded long-path laser absorption and laser induced fluorescence - Reply." Geophysical Research Letters **24,**23: 3039-3040, 1997.

Holland, F., M. Hessling and A. Hofzumahaus, "In-Situ Measurement of Tropospheric Oh Radicals by Laser-Induced Fluorescence - a Description of the Kfa Instrument." Journal of the Atmospheric Sciences **52,**19: 3393-3401, 1995.

Holland, F., A. Hofzumahaus, R. Schafer, A. Kraus and H. W. Patz, "Measurements of OH and HO2 radical concentrations and photolysis frequencies during BERLIOZ." Journal of Geophysical Research-Atmospheres **108,**D4, 2003.

Ivanov, A. V., S. Trakhtenberg, A. K. Bertram, Y. M. Gershenzon and M. J. Molina, "OH, HO2, and ozone gaseous diffusion coefficients." Journal of Physical Chemistry A **111,**9: 1632-1637, 2007.

Kukui, A., G. Ancellet and G. Le Bras, "Chemical ionisation mass spectrometer for measurements of OH and Peroxy radical concentrations in moderately polluted atmospheres." Journal of Atmospheric Chemistry **61,**2: 133-154, 2008.

Langhoff, S. R., E. F. Vandishoeck, R. Wetmore and A. Dalgarno, "Radiative Lifetimes and Dipole-Moments of the A2-Sigma+,B2-Sigma+, and C2-Sigma+ States of Oh." Journal of Chemical Physics **77,**3: 1379-1390, 1982.

Lelieveld, J., W. Peters, F. J. Dentener and M. C. Krol, "Stability of tropospheric hydroxyl chemistry." Journal of Geophysical Research-Atmospheres **107,**D23, 2002.

Mallik, C., L. Tomsche, E. Bourtsoukidis, J. N. Crowley, B. Derstroff, H. Fischer, S. Hafermann, I. Huser, U. Javed, S. Kessel, J. Lelieveld, M. Martinez, H. Meusel, A. Novelli, G. J. Phillips, A. Pozzer, A. Reiffs, R. Sander, D. Taraborrelli, C. Sauvage, J. Schuladen, H. Su, J. Williams and H. Harder, "Oxidation processes in the eastern Mediterranean atmosphere: evidence from the modelling of HOx measurements over Cyprus." Atmospheric Chemistry and Physics **18,**14: 10825-10847, 2018.

Mao, J., X. Ren, L. Zhang, D. M. Van Duin, R. C. Cohen, J. H. Park, A. H. Goldstein, F. Paulot, M. R. Beaver, J. D. Crounse, P. O. Wennberg, J. P. DiGangi, S. B. Henry, F. N. Keutsch, C. Park, G. W. Schade, G. M. Wolfe, J. A. Thornton and W. H. Brune, "Insights into hydroxyl measurements and atmospheric oxidation in a California forest." Atmospheric Chemistry and Physics **12,**17: 8009-8020, 2012.

Martinez, M., H. Harder, T. A. Kovacs, J. B. Simpas, J. Bassis, R. Lesher, W. H. Brune, G. J. Frost, E. J. Williams, C. A. Stroud, B. T. Jobson, J. M. Roberts, S. R. Hall, R. E. Shetter, B. Wert, A. Fried, B. Alicke, J. Stutz, V. L. Young, A. B. White and R. J. Zamora, "OH and HO2 concentrations, sources, and loss rates during the Southern Oxidants Study in Nashville, Tennessee, summer 1999." Journal of Geophysical Research-Atmospheres **108,**D19, 2003.

Martinez, M., H. Harder, D. Kubistin, M. Rudolf, H. Bozem, G. Eerdekens, H. Fischer, T. Klupfel, C. Gurk, R. Konigstedt, U. Parchatka, C. L. Schiller, A. Stickler, J. Williams and J. Lelieveld, "Hydroxyl radicals in the tropical troposphere over the Suriname rainforest: airborne measurements." Atmospheric Chemistry and Physics **10,**8: 3759-3773, 2010.

Mather, J. H., P. S. Stevens and W. H. Brune, "OH and HO2 measurements using laser-induced fluorescence." Journal of Geophysical Research-Atmospheres **102,**D5: 6427-6436, 1997.

Mauldin, R. L., E. Kosciuch, B. Henry, F. L. Eisele, R. Shetter, B. Lefer, G. Chen, D. Davis, G. Huey and D. Tanner, "Measurements of OH, HO2+RO2, H2SO4, and MSA at the south pole during ISCAT 2000." Atmospheric Environment **38,**32: 5423-5437, 2004.

Novelli, A., K. Hens, C. T. Ernest, D. Kubistin, E. Regelin, T. Elste, C. Plass-Dulmer, M. Martinez, J. Lelieveld and H. Harder, "Characterisation of an inlet pre-injector laser-induced fluorescence instrument for the measurement of atmospheric hydroxyl radicals." Atmospheric Measurement Techniques **7,**10: 3413-3430, 2014.

Regelin, E., H. Harder, M. Martinez, D. Kubistin, C. T. Ernest, H. Bozem, T. Klippel, Z. Hosaynali-Beygi, H. Fischer, R. Sander, P. Jockel, R. Konigstedt and J. Lelieveld, "HOx measurements in the summertime upper troposphere over Europe: a comparison of observations to a box model and a 3-D model." Atmospheric Chemistry and Physics **13,**21: 10703-10720, 2013.

Ren, X. R., H. Harder, M. Martinez, R. L. Lesher, A. Oliger, J. B. Simpas, W. H. Brune, J. J. Schwab, K. L. Demerjian, Y. He, X. L. Zhou and H. G. Gao, "OH and HO2 chemistry in the urban atmosphere of New York City." Atmospheric Environment **37,**26: 3639-3651, 2003.

Roach, P. E., "The Generation of Nearly Isotropic Turbulence by Means of Grids." International Journal of Heat and Fluid Flow **8,**2: 82-92, 1987.

Sander, S. P., B. J. Finlayson-Pitts, R. R. Friedl, D. M. Golden, R. E. Huie, C. E. Kolb, M. J. Kurylo, M. J. Molina, G. K. Moortgat, V. L. Orkin and A. R. Ravishankara, "Chemical Kinetics and Photochemical Data for Use in Atmospheric Studies." JPL Publication 02-25, 2003.

Schlosser, E., B. Bohn, T. Brauers, H. P. Dorn, H. Fuchs, R. Haseler, A. Hofzumahaus, F. Holland, F. Rohrer, L. O. Rupp, M. Siese, R. Tillmann and A. Wahner, "Intercomparison of two hydroxyl radical measurement techniques at the atmosphere simulation chamber SAPHIR." Journal of Atmospheric Chemistry **56,**2: 187-205, 2007.

Schlosser, E., T. Brauers, H. P. Dorn, H. Fuchs, R. Haseler, A. Hofzumahaus, F. Holland, A. Wahner, Y. Kanaya, Y. Kajii, K. Miyamoto, S. Nishida, K. Watanabe, A. Yoshino, D. Kubistin, M. Martinez, M. Rudolf, H. Harder, H. Berresheim, T. Elste, C. Plass-Dulmer, G. Stange and U. Schurath, "Technical Note: Formal blind intercomparison of OH measurements: results from the international campaign HOxComp." Atmospheric Chemistry and Physics **9,**20: 7923-7948, 2009.

Sjostedt, S. J., L. G. Huey, D. J. Tanner, J. Peischl, G. Chen, J. E. Dibb, B. Lefer, M. A. Hutterli, A. J. Beyersdorf, N. J. Blake, D. R. Blake, D. Sueper, T. Ryerson, J. Burkhart and A. Stohl, "Observations of hydroxyl and the sum of peroxy radicals at Summit, Greenland during summer 2003." Atmospheric Environment **41,**24: 5122-5137, 2007.

Smith, S. C., J. D. Lee, W. J. Bloss, G. P. Johnson, T. Ingham and D. E. Heard, "Concentrations of OH and HO2 radicals during NAMBLEX: measurements and steady state analysis." Atmospheric Chemistry and Physics **6**: 1435-1453, 2006.

Stevens, P. S., J. H. Mather and W. H. Brune, "Measurement of Tropospheric OH and $HO_2$ by Laser-Induced Fluorescence at Low-Pressure." Journal of Geophysical Research-Atmospheres **99,**D2: 3543-3557, 1994.

Stone, D., M. J. Evans, R. Commane, T. Ingham, C. F. A. Floquet, J. B. McQuaid, D. M. Brookes, P. S. Monks, R. Purvis, J. F. Hamilton, J. Hopkins, J. Lee, A. C. Lewis, D. Stewart, J. G. Murphy, G. Mills, D. Oram, C. E. Reeves and D. E. Heard, "HOx observations over West Africa during AMMA: impact of isoprene and NOx." Atmospheric Chemistry and Physics **10,**19: 9415-9429, 2010.

Tang, M. J., R. A. Cox and M. Kalberer, "Compilation and evaluation of gas phase diffusion coefficients of reactive trace gases in the atmosphere: volume 1. Inorganic compounds." Atmospheric Chemistry and Physics **14,**17: 9233-9247, 2014.

Tanner, D. J. and F. L. Eisele, "Present OH Measurement Limits and Associated Uncertainties." Journal of Geophysical Research-Atmospheres **100,**D2: 2883-2892, 1995.

Verreycken, T. and P. J. Bruggeman, "OH density measurements in nanosecond pulsed discharges in atmospheric pressure N-2-H2O mixtures." Plasma Sources Science & Technology **23,**1, 2014.

Winiberg, F. A. F., S. C. Smith, I. Bejan, C. A. Brumby, T. Ingham, T. L. Malkin, S. C. Orr, D. E. Heard and P. W. Seakins, "Pressure-dependent calibration of the OH and HO2 channels of a FAGE HOx instrument using the Highly Instrumented Reactor for Atmospheric Chemistry (HIRAC)." Atmospheric Measurement Techniques **8,**2: 523-540, 2015.

Zhang, D. H., M. A. Collins and S. Y. Lee, "First-principles theory for the H+H2O, D2O reactions." Science **290,**5493: 961-963, 2000.

**Seite 7: [1] Formatiert** **Marno, Daniel** **20.02.2020 12:21:00**

Schriftart: (Standard) +Textkörper (Calibri), 11 Pt., Englisch (Vereinigtes Königreich)

**Seite 7: [2] Formatiert** **Marno, Daniel** **20.02.2020 12:21:00**

Block

**Seite 7: [3] Formatiert** **Marno, Daniel** **03.02.2020 13:33:00**

Schriftart: Fett

**Seite 7: [4] Formatiert** **Marno, Daniel** **31.01.2020 15:55:00**

Schriftart: (Standard) Times New Roman, 8 Pt., Fett

**Seite 7: [5] Formatiert** **Marno, Daniel** **31.01.2020 15:55:00**

Zentriert

**Seite 7: [6] Formatiert** **Marno, Daniel** **31.01.2020 16:03:00**

Schriftart: (Standard) Times New Roman, 8 Pt., Fett, Englisch (Vereinigte Staaten)

**Seite 7: [7] Formatiert** **Marno, Daniel** **31.01.2020 15:55:00**

Schriftart: (Standard) Times New Roman, 8 Pt., Fett

**Seite 7: [8] Formatiert** **Marno, Daniel** **31.01.2020 15:55:00**

Schriftart: (Standard) Times New Roman, 8 Pt., Fett, Deutsch (Deutschland)

**Seite 7: [9] Formatiert** **Marno, Daniel** **31.01.2020 15:57:00**

Schriftart: 6 Pt.

**Seite 7: [10] Formatiert** **Marno, Daniel** **31.01.2020 15:55:00**

Zentriert

**Seite 7: [11] Formatiert** **Marno, Daniel** **31.01.2020 15:57:00**

Schriftart: 6 Pt.

**Seite 7: [12] Formatiert** **Marno, Daniel** **31.01.2020 15:58:00**

Schriftart: 8 Pt.

**Seite 7: [13] Formatiert** **Marno, Daniel** **31.01.2020 15:58:00**

Schriftart: 8 Pt.

**Seite 7: [14] Formatiert** **Marno, Daniel** **31.01.2020 15:57:00**

Schriftart: 6 Pt.

**Seite 7: [15] Formatiert** **Marno, Daniel** **31.01.2020 15:57:00**

Schriftart: (Standard) Times New Roman, 6 Pt., Fett, Deutsch (Deutschland)

**Seite 7: [16] Formatiert** **Marno, Daniel** **31.01.2020 15:55:00**

Zentriert

**Seite 7: [17] Formatiert** **Marno, Daniel** **31.01.2020 15:57:00**

Schriftart: 6 Pt.

**Seite 7: [18] Formatiert** **Marno, Daniel** **31.01.2020 15:59:00**

Schriftart: 8 Pt.

**Seite 7: [19] Formatiert** **Marno, Daniel** **31.01.2020 15:59:00**

Schriftart: 8 Pt.

**Seite 7: [20] Formatiert** **Marno, Daniel** **31.01.2020 15:57:00**

Schriftart: 6 Pt.

**Seite 7: [21] Formatiert** **Marno, Daniel** **31.01.2020 15:57:00**

Schriftart: (Standard) Times New Roman, 6 Pt., Fett, Deutsch (Deutschland)

**Seite 7: [22] Formatiert** **Marno, Daniel** **31.01.2020 15:55:00**

Zentriert

**Seite 7: [23] Formatiert** **Marno, Daniel** **31.01.2020 15:57:00**

Schriftart: 6 Pt.

**Seite 7: [24] Formatiert** **Marno, Daniel** **31.01.2020 15:57:00**

Schriftart: (Standard) Times New Roman, 6 Pt., Fett, Deutsch (Deutschland)

**Seite 7: [25] Formatiert** **Marno, Daniel** **31.01.2020 15:55:00**

Zentriert

**Seite 7: [26] Formatiert** **Marno, Daniel** **31.01.2020 15:57:00**

Schriftart: 6 Pt.

**Seite 7: [27] Formatiert** **Marno, Daniel** **31.01.2020 16:01:00**

Schriftart: 6 Pt.

**Seite 7: [28] Formatiert** **Marno, Daniel** **31.01.2020 16:01:00**

Schriftart: 6 Pt.

**Seite 7: [29] Formatiert** **Marno, Daniel** **31.01.2020 15:57:00**

Schriftart: 6 Pt.

**Seite 7: [30] Formatiert** **Marno, Daniel** **31.01.2020 15:57:00**

Schriftart: (Standard) Times New Roman, 6 Pt., Fett, Deutsch (Deutschland)

**Seite 7: [31] Formatiert** **Marno, Daniel** **31.01.2020 15:55:00**

Zentriert

**Seite 7: [32] Formatiert** **Marno, Daniel** **31.01.2020 15:55:00**

Schriftart: (Standard) Times New Roman, 8 Pt., Fett, Deutsch (Deutschland)

**Seite 8: [33] Formatiert** **Marno, Daniel** **20.02.2020 12:21:00**

Beschriftung, Block, Nicht vom nächsten Absatz trennen

**Seite 8: [34] Gelöscht** **Marno, Daniel** **30.01.2020 16:22:00**

**Seite 8: [35] Gelöscht** **Marno, Daniel** **30.01.2020 16:22:00**

**Seite 8: [36] Gelöscht** **Marno, Daniel** **31.01.2020 12:10:00**

**Seite 20: [37] Formatiert** **Marno, Daniel** **03.02.2020 09:35:00**

Schriftart: 11 Pt.

**Seite 20: [38] Formatiert** **Marno, Daniel** **03.02.2020 09:35:00**

Schriftart: 11 Pt.

**Seite 20: [39] Formatiert** **Marno, Daniel** **03.02.2020 09:35:00**

Schriftart: 11 Pt.

**Seite 20: [40] Formatiert** **Marno, Daniel** **03.02.2020 09:35:00**

Schriftart: 11 Pt.

**Seite 20: [41] Formatiert** **Marno, Daniel** **03.02.2020 09:35:00**

Schriftart: 11 Pt.

**Seite 20: [42] Formatiert** **Marno, Daniel** **03.02.2020 09:35:00**

Schriftart: 11 Pt.

**Seite 20: [43] Formatiert** **Marno, Daniel** **03.02.2020 09:35:00**

Schriftart: 11 Pt.

**Seite 20: [44] Formatiert** **Marno, Daniel** **03.02.2020 09:35:00**

Schriftart: 11 Pt.

**Seite 20: [45] Formatiert** **Marno, Daniel** **03.02.2020 09:35:00**

Schriftart: 11 Pt.

**Seite 20: [46] Formatiert** **Marno, Daniel** **03.02.2020 09:35:00**

Schriftart: 11 Pt.

**Seite 20: [47] Formatiert** **Marno, Daniel** **03.02.2020 09:35:00**

Schriftart: 11 Pt.

**Seite 20: [48] Formatiert** **Marno, Daniel** **03.02.2020 09:35:00**

Schriftart: 11 Pt.

**Seite 20: [49] Formatiert** **Marno, Daniel** **03.02.2020 09:35:00**

Schriftart: 11 Pt.

**Seite 20: [50] Formatiert** **Marno, Daniel** **03.02.2020 09:35:00**

Schriftart: 11 Pt.

**Seite 20: [51] Formatiert** **Marno, Daniel** **03.02.2020 09:35:00**

Schriftart: 11 Pt.

**Seite 20: [52] Formatiert** **Marno, Daniel** **03.02.2020 09:35:00**

Schriftart: 11 Pt.

**Seite 20: [53] Formatiert** **Marno, Daniel** **03.02.2020 09:35:00**

Schriftart: 11 Pt.

**Seite 20: [54] Formatiert** **Marno, Daniel** **03.02.2020 09:35:00**

Schriftart: 11 Pt.

**Seite 20: [55] Formatiert** **Marno, Daniel** **03.02.2020 09:35:00**

Schriftart: 11 Pt.

**Seite 20: [56] Formatiert** **Marno, Daniel** **03.02.2020 09:35:00**

Schriftart: 11 Pt.

**Seite 20: [57] Formatiert** **Marno, Daniel** **03.02.2020 09:35:00**

Schriftart: 11 Pt.

**Seite 20: [58] Formatiert** **Marno, Daniel** **03.02.2020 09:35:00**

Schriftart: 11 Pt.

**Seite 20: [59] Formatiert** **Marno, Daniel** **03.02.2020 09:35:00**

Schriftart: 11 Pt.

**Seite 20: [60] Formatiert** **Marno, Daniel** **20.02.2020 12:21:00**

Einzug: Erste Zeile: 0 cm

**Seite 20: [61] Gelöscht** **Marno, Daniel** **25.02.2020 16:44:00**

**Seite 20: [61] Gelöscht** **Marno, Daniel** **25.02.2020 16:44:00**

**Seite 20: [62] Gelöscht** **Marno, Daniel** **17.01.2020 12:03:00**

**Seite 20: [62] Gelöscht** **Marno, Daniel** **17.01.2020 12:03:00**

**Seite 20: [62] Gelöscht** **Marno, Daniel** **17.01.2020 12:03:00**

**Seite 20: [62] Gelöscht** **Marno, Daniel** **17.01.2020 12:03:00**

**Seite 20: [62] Gelöscht** **Marno, Daniel** **17.01.2020 12:03:00**

**Seite 20: [62] Gelöscht** **Marno, Daniel** **17.01.2020 12:03:00**

**Seite 20: [62] Gelöscht** **Marno, Daniel** **17.01.2020 12:03:00**

**Seite 20: [62] Gelöscht** **Marno, Daniel** **17.01.2020 12:03:00**

**Seite 20: [63] Gelöscht** **Marno, Daniel** **16.01.2020 13:05:00**

**Seite 20: [63] Gelöscht** **Marno, Daniel** **16.01.2020 13:05:00**

**Seite 20: [63] Gelöscht** **Marno, Daniel** **16.01.2020 13:05:00**

**Seite 20: [64] Formatiert** **Marno, Daniel** **20.02.2020 12:21:00**

Einzug: Erste Zeile: 0,5 cm

**Seite 20: [65] Formatiert** **Marno, Daniel** **20.02.2020 12:21:00**

Block

**Seite 20: [66] Formatiert** **Marno, Daniel** **03.02.2020 09:35:00**

Schriftart: 11 Pt.

**Seite 20: [67] Gelöscht** **Marno, Daniel** **03.02.2020 09:42:00**

**Seite 20: [67] Gelöscht** **Marno, Daniel** **03.02.2020 09:42:00**

**Seite 20: [68] Formatiert** **Marno, Daniel** **03.02.2020 09:35:00**

Schriftart: 11 Pt.

**Seite 20: [69] Formatiert** **Marno, Daniel** **03.02.2020 09:35:00**

Schriftart: 11 Pt.

**Seite 20: [70] Formatiert** **Marno, Daniel** **20.02.2020 12:21:00**

Block

**Seite 20: [71] Formatiert** **Marno, Daniel** **03.02.2020 09:35:00**

Schriftart: 11 Pt.

**Seite 20: [72] Formatiert** **Marno, Daniel** **03.02.2020 09:35:00**

Schriftart: 11 Pt.

**Seite 20: [73] Formatiert** **Marno, Daniel** **20.02.2020 12:21:00**

Block

**Seite 20: [74] Formatiert** **Marno, Daniel** **03.02.2020 09:35:00**

Schriftart: 11 Pt.

**Seite 25: [75] Formatiert** **Marno, Daniel** **03.02.2020 09:35:00**

Schriftart: 11 Pt.

**Seite 25: [76] Formatiert** **Marno, Daniel** **20.02.2020 12:21:00**

Block

**Seite 25: [77] Formatiert** **Marno, Daniel** **03.02.2020 09:35:00**

Schriftart: 11 Pt.

**Seite 25: [78] Formatiert** **Marno, Daniel** **20.02.2020 12:21:00**

Block

**Seite 25: [79] Formatiert** **Marno, Daniel** **03.02.2020 09:35:00**

Schriftart: 11 Pt.

**Seite 25: [80] Formatiert** **Marno, Daniel** **03.02.2020 09:35:00**

Schriftart: 11 Pt.

**Seite 25: [81] Formatiert** **Marno, Daniel** **03.02.2020 09:35:00**

Schriftart: 11 Pt.

**Seite 25: [82] Formatiert** **Marno, Daniel** **03.02.2020 09:35:00**

Schriftart: 11 Pt.

**Seite 25: [83] Formatiert** **Marno, Daniel** **20.02.2020 12:21:00**

Block

**Seite 25: [84] Formatiert** **Marno, Daniel** **03.02.2020 09:35:00**

Schriftart: 11 Pt.

**Seite 25: [85] Formatiert** **Marno, Daniel** **03.02.2020 09:35:00**

Schriftart: 11 Pt.

**Seite 25: [86] Formatiert** **Marno, Daniel** **03.02.2020 09:35:00**

Schriftart: 11 Pt.

**Seite 25: [87] Formatiert** **Marno, Daniel** **20.02.2020 12:21:00**

Block

**Seite 25: [88] Formatiert** **Marno, Daniel** **03.02.2020 09:35:00**

Schriftart: 11 Pt.

**Seite 25: [89] Formatiert** **Marno, Daniel** **03.02.2020 09:35:00**

Schriftart: 11 Pt.

**Seite 25: [90] Formatiert** **Marno, Daniel** **03.02.2020 09:35:00**

Schriftart: 11 Pt.

**Seite 25: [91] Formatiert** **Marno, Daniel** **03.02.2020 09:35:00**

Schriftart: 11 Pt.

**Seite 25: [92] Formatiert** **Marno, Daniel** **20.02.2020 12:21:00**

Block

**Seite 25: [93] Formatiert** **Marno, Daniel** **29.01.2020 10:44:00**

Schriftart: (Standard) Times New Roman, 12 Pt.

**Seite 25: [94] Formatiert** **Marno, Daniel** **20.02.2020 12:21:00**

Block, Einzug: Erste Zeile: 0,5 cm

**Seite 25: [95] Formatiert** **Marno, Daniel** **29.01.2020 10:44:00**

Schriftart: (Standard) Times New Roman, 12 Pt.

**Seite 25: [96] Formatiert** **Marno, Daniel** **29.01.2020 10:44:00**

Schriftart: (Standard) Times New Roman, 12 Pt.

**Seite 25: [97] Formatiert** **Marno, Daniel** **03.02.2020 09:36:00**

Schriftart: 11 Pt.

**Seite 25: [98] Formatiert** **Marno, Daniel** **20.02.2020 12:21:00**

Block

**Seite 25: [99] Formatiert** **Marno, Daniel** **03.02.2020 09:36:00**

Schriftart: 11 Pt.

**Seite 25: [100] Formatiert** **Marno, Daniel** **20.02.2020 12:21:00**

Block

**Seite 25: [101] Formatiert** **Marno, Daniel** **03.02.2020 09:36:00**

Schriftart: 11 Pt.

**Seite 25: [102] Formatiert** **Marno, Daniel** **20.02.2020 12:21:00**

Block

**Seite 25: [103] Formatiert** **Marno, Daniel** **03.02.2020 09:36:00**

Schriftart: 11 Pt.

**Seite 25: [104] Formatiert** **Marno, Daniel** **20.02.2020 12:21:00**

Block

**Seite 25: [105] Formatiert** **Marno, Daniel** **25.02.2020 16:18:00**

Schriftart: Kursiv, Tiefgestellt

**Seite 27: [106] Gelöscht** **Marno, Daniel** **12.02.2020 16:58:00**